COMENIUS UNIVERSITY IN BRATISLAVA
FACULTY OF MATHEMATICS, PHYSICS AND INFORMATICS

STUDY OF NUCLEAR STRUCTURE AND BEYOND THE STANDARD MODEL PHYSICS BY INVESTIGATION OF $2\nu\beta\beta$ DIFFERENTIAL CHARACTERISTICS WITHIN THE SUPERNEMO EXPERIMENT

ESSAY FOR DOCTORAL THESIS

2023
MGR. MAROŠ PETRO

Comenius University in Bratislava
Faculty of Mathematics, Physics and Informatics

Study of nuclear structure and beyond the Standard Model Physics by investigation of $2\nu\beta\beta$ differential characteristics within the SuperNEMO experiment

Essay for Doctoral Thesis

Study Programme:	Physics
Field of Study:	Nuclear and Subnuclear Physics
Department:	Department of Nuclear Physics and Biophysics
Supervisor:	prof. RNDr. Fedor Šimkovic, CSc.
Consultant:	Mgr. Miroslav Macko, Ph.D.

Bratislava, 2023
Mgr. Maroš Petro

Declaration of Honor:

I hereby declare on my honor that I personally elaborated the study presented here, under leadership of my supervisor and with assistance of my consultant. Literature and sources are listed.

Prague, August 2023

Mgr. Maroš Petro

CONTENTS

LIST OF FIGURES

INTRODUCTION

The two neutrino double beta decay ($2\nu\beta\beta$) is an extremely rare type of nuclear decay. This process was postulated in Goeppert-Mayer in 1935 [1]. In $2\nu\beta\beta$ two neutrons are simultaneously transformed into two protons accompanied by an emission of two electrons and two anti-neutrinos. Typically, the half-life for various measured isotopes that undergo this type of decay exceeds $10^{18}y$. The study of neutrino properties (such as neutrino mass scale, neutrino nature or the lepton number conservation) is closely tied to the double beta decay (DBD) processes. Most experiments today, however, focus on a different mode called the neutrinoless double beta decay ($0\nu\beta\beta$). This hypothetical process, if it occurs, violates the lepton number conservation as no neutrinos are emitted in the decay. It can serve as direct tool for the study of absolute neutrino mass scale and its nature (whether Dirac or Majorana).

Efforts to detect $0\nu\beta\beta$ have greatly advanced the detection technologies, which are exploited by many modern experiments (i.e. LEGEND [2], KamLAND-Zen [3]). One of these modern experiments is the SuperNEMO experiment. SuperNEMO is a unique experiment employing calorimetry combined with particle trajectory tracking, allowing measurements of full decay characteristics generally not accessible in other experiments. These include the measurements of single electron energy spectra and angular distributions of the opening angle between the two electrons.

SuperNEMO's (and that of other DBD experiments) primary aim is the detection of $0\nu\beta\beta$, but since the decay remains elusive, many theoretical physicists are revisiting $2\nu\beta\beta$. Some predictions, like those in [4, 5], describe the $2\nu\beta\beta$ spectrum more precisely, impacting calculations of nuclear matrix elements, influencing the calculation of $0\nu\beta\beta$ half-life. Additionally, Beyond Standard Model processes involving right-handed neutrino currents or sterile neutrinos, as proposed in [6] and [7] respectivelly, could provide insights into neutrino properties through the study of $2\nu\beta\beta$ spectral shapes. Such approach has not yet been taken before.

A common need across these studies is the precise examination of $2\nu\beta\beta$ spectra.

While most experiments can only measure the sum of electron energies in the decay, SuperNEMO's additional observables like single-electron energies and opening angles between electrons should prove superior in this type of investigation. Whether these observables can contribute to understanding new physics questions remains uncertain, however.

This Ph.D. thesis aims to investigate SuperNEMO's capabilities for studying new physics, particularly focusing on angular distribution measurements (or combination of angular and single electron energy distributions) and evaluating the potential use of SuperNEMO in exploring new aspects of $2\nu\beta\beta$ physics.

CHAPTER 1

NEUTRINO PROPERTIES AND OPENED QUESTIONS

1.1 Throughout the 20^{th} Century

1.1.1 Neutrino Postulate

In the 1920s, early measurements of β-decay demonstrated a continuous electron energy spectrum with an endpoint at the Q-value of the reaction (see Figure 1.1). This finding was unexpected as it was originally believed that β-decay would be a two-body process, similar to α-decay, where the parent nucleus ${}^{A}_{Z}X$ decays into a daughter nucleus ${}^{A}_{Z-1}Y$ with the emission of an electron:

$$
{}^{A}_{Z}X \longrightarrow {}^{A}_{Z-1}Y + e^{-}. \tag{1.1}
$$

The continuous spectrum observed in β-decay challenged various fundamental conservation laws, including energy and momentum conservation. To address this issue, Pauli proposed in 1930 that the decay is actually a three-body process, involving the emission of an ”undetectable” particle alongside the electron. His proposal was carried out in a letter which he wrote for Tübingen Conference, the translation of the letter is given in [8]. This particle was later named the ”neutrino” by E. Fermi, meaning ”the small neutral one.”

With the inclusion of the neutrino in the decay process, energy conservation could be achieved, allowing the decay energy to be distributed between the electron and the neutrino. The neutrino was assumed to have an extremely small mass. Therefore, the endpoint of the measured electron energy spectrum would be bent in a concave shape depending on the neutrino mass. In order to preserve charge in the decay, the neutrino had to be electromagnetically neutral. Additionally, the neutrino was assigned a spin of 1/2 to ensure the conservation of total angular momentum. The need for the half-integer spin of the neutrino can be shown, for example, in the decay of nuclei with

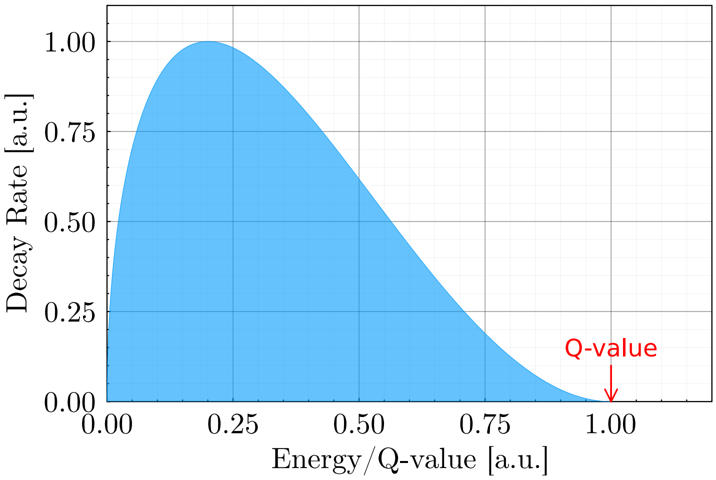

Figure 1.1: Schematic view of the β-decay spectrum. The Q-value is indicated as the endpoint of the spectrum.

even number of nucleons (A). In the β-decay, A remains unchanged, so both the parent and the daughter nuclei must have integer or half-integer nuclear spin. An emission of only an electron, with half-integer spin, would violate the conservation of angular momentum. Finally, to conserve the lepton number (LN), it is an anti-neutrino that (as opposed to neutrino) which has to be emitted alongside the electron [9]. The equation (1.1) can be rewritten in the proper form as follows:

$$ {}^{A}_{Z}X \longrightarrow {}^{A}_{Z-1}Y + e^{-} + \bar{\nu}. \tag{1.2}$$

1.1.2 First Neutrino Observation

In 1934, Fermi developed a quantitative theory of β-decay. He incorporated the neutrino into the decay calculations. One of the successes of his theory was the prediction of the existence of so-called inverse β-decay process. In this decay, an anti-neutrino is captured by a proton, resulting in the conversion of the proton into a neutron and the emission of a positron:

$$\bar{\nu} + p^{+} \longrightarrow n^{0} + e^{+}. \tag{1.3}$$

In 1956, Cowan and Reines exploited this process to provide the first experimental evidence for the existence of neutrinos. In their experiment, they used a nuclear reactor as a potent source of anti-neutrinos. Their detector consisted of two large (200 l) tanks filled with a mixture of water and cadmium chloride, sandwiched between three layers of scintillating detectors.

A schematic view of the detector is shown in Figure 1.2. Water was used as a medium to increase the number of potential target protons for the reaction. Cadmium

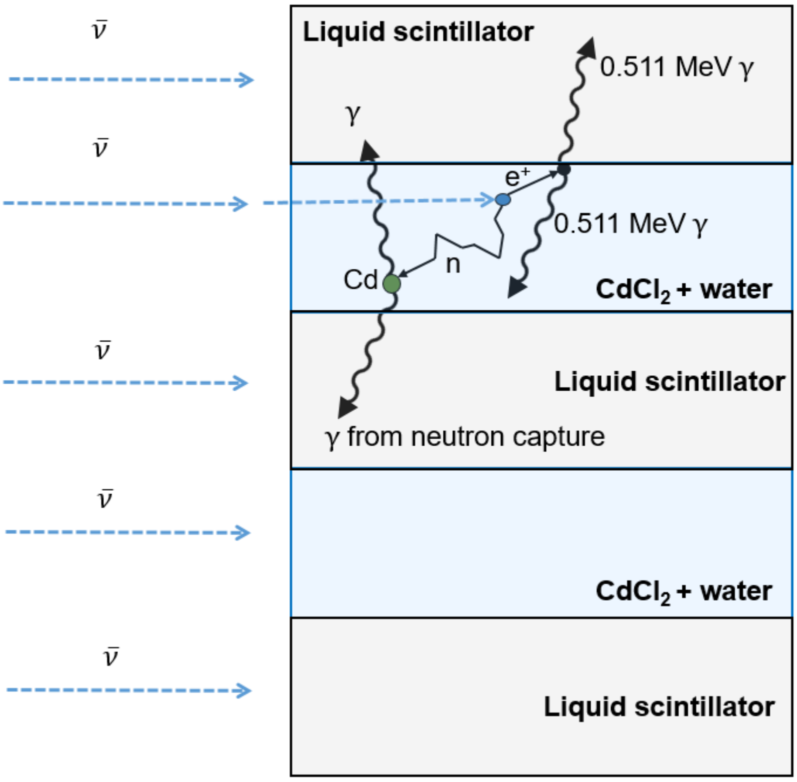

Figure 1.2: Schematic view of Cowan-Reines experimental setup for detection of anti-neutrinos. From [10].

chloride ($CdCl_2$) was dissolved in the water to facilitate the capture of the neutrons as cadmium has a large neutron capture cross-section.

The experimental signature of the decay manifested itself in form of two distinct signals. First, two 511 keV γ-rays are detected as a result of electron-positron annihilation. Second, a delayed γ-ray is detected from the neutron capture on cadmium (and subsequent deexcitation). The combination of these two signatures provided Cowan and Reines with a clear signal to look for. In 1956, Cowan and Reines published their results [11]. Subsequently, Reines was awarded the Nobel Prize in Physics in 1995. A simplified schema of the experiment is shown in the Figure 1.2.

1.2 Neutrino Properties

1.2.1 Neutrino Flavors, Oscillations and Masses

Within the Standard Model (SM) neutrinos are assumed to be massless neutral leptons which come in three so-called flavors. These are the electron-neutrino (ν_e), muon-neutrino (ν_μ) and tau-neutrino (ν_τ). The flavor defines so-called interaction states of neutrinos. They are defined based on the charge leptons (e, μ, τ) along with which the neutrino is created in the weak interactions. The definition of flavors is necessary due to the fact that the neutrinos can only be detected indirectly, based on the presence of their charged lepton partner. Today we know that there can only be three weakly interacting states of neutrinos. This was proven by the measurements of the decay width of the Z^0 gauge boson [12].

Thanks to the discovery of neutrino oscillations [13, 14] we now know neutrinos are not massless. The SM recognizes three neutrino mass eigenstates, denoted by ν_1, ν_2, ν_3. The concept of neutrino oscillations is based on the fact that the neutrino mass eigenstate and flavor eigenstate do not match exactly. The three neutrino flavors, within the SM, can be written as a linear combination of the neutrino mass eigenstates. The unitary transformation between the two bases is given by:

$$|\nu_\alpha\rangle = \sum_i U_{\alpha i} |\nu_i\rangle , \tag{1.4}$$

$$|\nu_i\rangle = \sum_\alpha U^*_{\alpha i} |\nu_\alpha\rangle . \tag{1.5}$$

Where $U_{\alpha i}$ are the matrix elements of the Pontecorvo – Maki – Nakagawa – Sakata (PMNS) matrix. The mixing between the two bases give rise to so-called the neutrino flavor oscillations – a phenomenon in which a neutrino created in a particular flavor state can be measured in a different flavor as it propagates through vacuum. If one considers a simplified case of mixing of two neutrino flavors, the PMNS matrix takes form of a 2×2 matrix. The probability to change flavors from one flavor eigenstate (ν_α) to another (ν_β) is given as (derived in [15]):

$$P(\nu_\alpha \rightarrow \nu_\beta) = sin^2(2\theta) sin^2 \left(\frac{\Delta m^2_{ij} L}{4E} \right) . \tag{1.6}$$

Here, L is the distance the neutrino has travelled in vacuum, E is kinetic energy of the neutrino, θ is the neutrino mixing angle, and $\Delta m^2_{ij} = m^2_i - m^2_j$ is the mass squared difference of the i-th and j-th neutrino mass eigenstates. From this relation it is obvious that the neutrino oscillations can only occur only if $\theta \neq 0$ and $\Delta m^2_{ij} \neq 0$ simultaneously. This means that existence of neutrino oscillations prove that the neutrinos are mixing and that at least two neutrino mass states have nonzero mass.

This consequence was exploited in a number of neutrino oscillation experiments. The first to confirm that neutrinos oscillate were experiments at the Super-Kamiokande Observatory [16] and Sudbury Neutrino Observatory [17]. In 2015, Takaaki Kajita (for Super-Kamiokande) and Arthur McDonald (for Sudbury Neutrino Observatory) received a Nobel Prize in physics.

A question arises, however, if neutrinos are not all massless, what is their mass? The non-zero value of Δm^2_{ij} does not give information about the specific values of m_i or

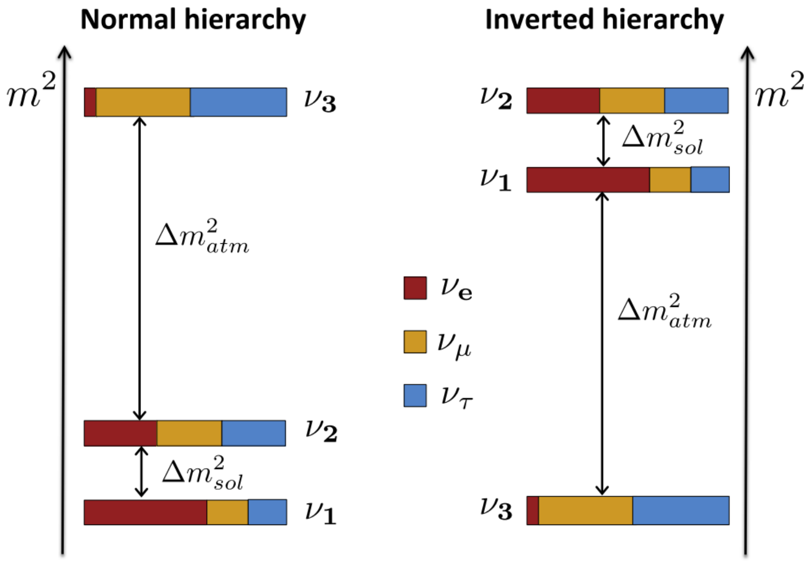

Figure 1.3: Schematic view of Normal (left) and Inverted (right) neutrino mass ordering. From [19].

m_j. The labeling of individual mass eigenstates is determined by their primary coupling to specific flavor eigenstates, following a rule where the mass eigenstate predominantly associated with a particular flavor eigenstate receives a specific label. It should be noted that this labeling does not imply ordering based on the masses of the neutrinos. It is unknown which neutrino mass eigenstate is the lightest or heaviest. This is the so-called *Neutrino Mass Hierarchy* problem. There are two possibilities for how the neutrino masses are ordered. It is known that $\Delta m^2_{12} > 0$, thus $m_1 < m_2$, the sign of Δm^2_{31} is unknown [18]. One possible ordering is if $m_1 < m_2 < m_3$, a so-called normal ordering is obtained. Otherwise, if $m_3 < m_1 < m_2$ the so-called inverted ordering is realized.

Figure 1.3 depicts the two possibilities. Current experimental measurements have determined the squared mass differences of neutrino mass eigenstates as $|\Delta m^2_{31}| = |m^2_3 - m^2_1| \approx 2.5 \cdot 10^{-3}\text{eV}^2$ and $\Delta m^2_{21} = m^2_2 - m^2_1 \approx 7.39 \cdot 10^{-5}\text{eV}^2$ [20].

1.2.2 Neutrino Mass Mechanisms and Neutrino Nature

To explain non-zero neutrino masses, one must go beyond the SM. The description of how neutrino masses are generated is closely tied to the question of their nature. If neutrino is distinguishable from an anti-neutrino (so-called Dirac particle), its mass can be included into the theory using the so-called Dirac mass term. Including both the so-called left-handed (ν_L) and right-handed (ν_R) neutrino fields, with:

$$\nu_L = \begin{pmatrix} \nu_{eL} \\ \nu_{\mu L} \\ \nu_{\tau L} \\ \dots \end{pmatrix}, \; \nu_R = \begin{pmatrix} \nu_{eR} \\ \nu_{\mu R} \\ \nu_{\tau R} \\ \dots \end{pmatrix},$$

the SM Lagrangian can be extended with the Dirac mass term (M^D) as shown in [21]:

$$\mathcal{L}_D = -\bar{\nu}_R M^D \nu_L + \text{h.c.} \tag{1.7}$$

In this representation, the particles and antiparticles do not mix, and LN is conserved. However, it introduces right-handed neutrinos that are completely non-interacting within the SM [12].

On the other hand, if neutrinos are so-called Majorana particles, i.e. a neutrino and an anti-neutrino are described by identical field but with opposite chiralities, the Lagrangian can be constructed as follows [21]:

$$\mathcal{L}_M = -\bar{\nu}_L^C M^M \nu_L + \text{h.c.} \tag{1.8}$$

Here, $\bar{\nu}^C$ represents the neutrino charge conjugate, and M_M is the Majorana mass term. This mechanism was originally proposed by Majorana in 1937 [22]. If neutrinos were indeed Majorana particles, processes violating LN would be allowed (further discussed in section 2.2).

Lastly, the most general case involves the so-called Dirac-Majorana mass term. Here, the Lagrangian takes the form of:

$$\mathcal{L}_{D+M} = -\frac{1}{2}\bar{\nu_L}^C M_L^M \nu_L - \frac{1}{2}\bar{\nu_R} M_R^M (\nu_R)^C - \bar{\nu_R} M^D \nu_L + \text{h.c.} \tag{1.9}$$

1.2.3 Some of the Opened Questions in Neutrino Physics

Neutrinos are the most elusive particles that constitute the matter of the Universe. This is the reason why neutrino experiments need to combine immense effort from both the theoretical and the experimental physicists. There are still numerous complex questions regarding their properties that require further investigation. As mentioned earlier, one such question is the neutrino mass hierarchy, which relates to the arrangement of neutrino mass eigenstates and the identification of the lightest among them. Currently, our knowledge is constrained to measurements of mass squared differences, and the absolute mass scale of neutrinos remains unknown. Although experiments have established upper limits on neutrino masses, these limits are discussed in greater detail in section 2.3.

Furthermore, the nature of neutrinos is still not fully understood. It remains uncertain whether they are Dirac or Majorana particles. In the case of Dirac nature, the neutrino consists of left- and right-handed fields. However, in the case of Majorana nature, the neutrino consists of the left-handed field and its charge conjugate.

Apart from these fundamental questions, there are several other unresolved aspects. One intriguing possibility is the existence of sterile neutrinos, which are hypothesized to not interact via the Weak force and only experience the Gravity. Double beta decay (DBD) is a promising avenue for investigating the unknown neutrino properties and exploring possible extensions beyond the Standard Model.

CHAPTER 2

DOUBLE BETA DECAY

2.1 Two-Neutrino Double Beta Decay

Two-neutrino double beta decay ($2\nu\beta\beta$) is a process proposed by Goeppert-Mayer in 1935 [1]. In this process two nucleons within the nucleus undergo a transition with emission of two beta particles and two anti-neutrinos. Thus $2\nu\beta\beta$ keeps nucleon mass number A constant. To describe the binding energy B of nucleons within the nucleus, the Bethe–Weizsäcker mass formula can be used:

$$B(Z, A) = a_V A - a_S A^{2/3} - a_C \frac{Z(Z-1)}{A^{1/3}} - a_A \frac{(N-Z)^2}{A} + \delta_P. \tag{2.1}$$

For isobars (nuclei with the same mass number A, but different proton number Z) the Bethe–Weizsäcker mass formula can be reduced to a function of Z as:

$$B(Z, A = \mathit{constant}) \propto \mathit{constant} + \alpha Z + \beta Z^2 + \delta_P, \tag{2.2}$$

where α and β are constants, and the pairing term δ_P is:

$$\delta_P = \begin{cases} -a_P A^{-1/2} & \text{even-even nuclei} \\ 0 & \text{even-odd and odd-even nuclei} \\ +a_P A^{-1/2} & \text{odd-odd nuclei} \end{cases} \tag{2.3}$$

As a consequence of the pairing term, there are two possibilities for mass parabolas for isobars. When A is odd, a single mass parabola is obtained because $\delta_P = 0$. A more interesting case, however, happens when A is even. For even A nuclei $\delta_P = \pm a_P A^{-1/2}$, two mass parabolas are obtained, separated by $2\delta_P$. Figure 2.1 shows an example of two mass parabolas calculated using (2.2) for an even A nucleus. It can be seen that the transition of $|\Delta Z| = 1$ is energetically forbidden. On the other hand, a transition with $|\Delta Z| = 2$ is energetically allowed.

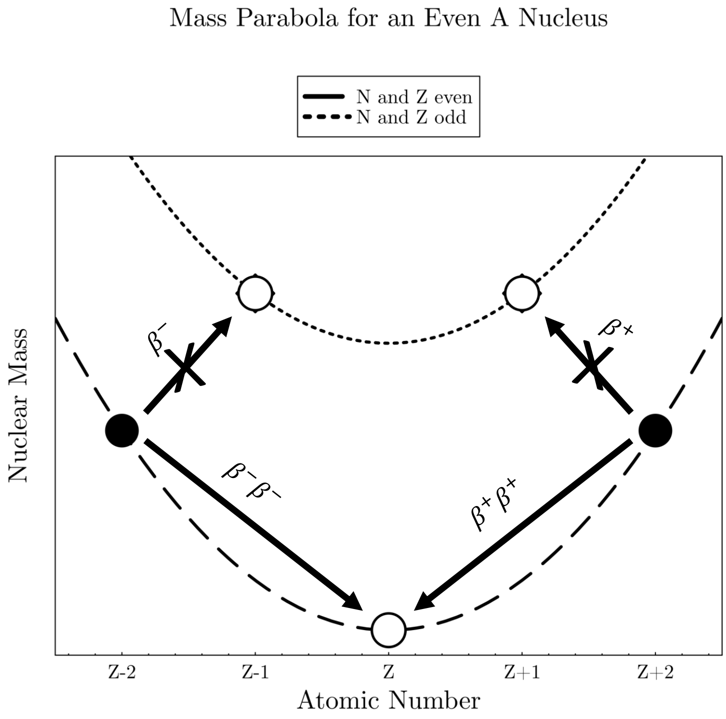

Figure 2.1: Mass parabolas for a nucleus of even A. The possible and forbidden decay modes are marked by arrows.

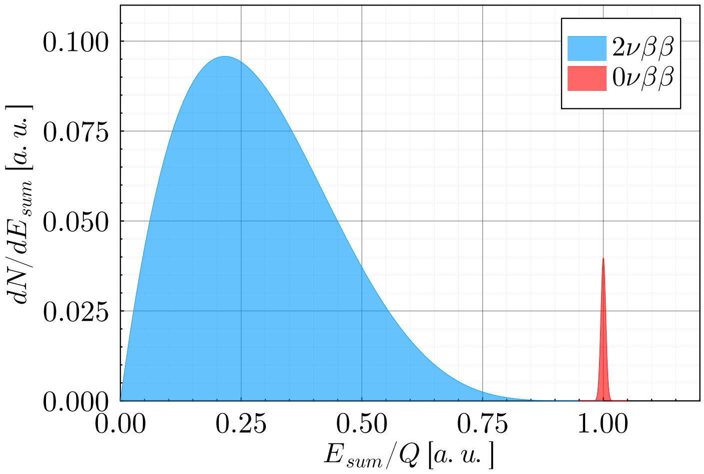

Figure 2.2: A typical shape of the $2\nu\beta\beta$ spectrum in blue and of $0\nu\beta\beta$ in red. The x-axis represents the sum of electron energies E_{sum} divided by the Q-value of the reaction. Peaks are smeared to represent a measurement with finite energy resolution.

It is important to note that while transitions with $|\Delta Z| = 2$ are possible for various isotopes, experimentally viable cases are limited to even-even nuclei with forbidden ordinary β-decay. This constraint arises because ordinary β-decay processes would obscure the experimental signature of double-beta decay. There are 35 candidate isotopes for $2\nu\beta\beta$ ($0^+ \to 0^+$, ground state transition) [23]. So far, $2\nu\beta\beta$ has been observed for 11 isotopes and $2\nu EC/EC$ for 3 isotopes. These are listed in [24].

Goeppert-Mayer originally proposed the existence of double beta decay (DBD), where two neutrons within a nucleus spontaneously transform into two protons, releasing two electrons and two antineutrinos, the decay is labeled $2\nu\beta^-\beta^-$:

$$2\nu\beta^-\beta^- : \quad (Z, A) \to (Z+2, A) + 2e^- + 2\bar{\nu}_e. \tag{2.4}$$

Furthermore, three additional modes of $2\nu\beta\beta$ exist. In $2\nu\beta^+\beta^+$, two protons are transformed into two neutrons with emission of two positrons and two neutrinos. In $2\nu\beta^+/EC$ an electron from atomic shell is captured by the nucleus, a positron and two neutrinos are emitted. Lastly, in $2\nu EC/EC$ two electrons from atomic shell are captured and two neutrinos emitted. Equations (2.5) - (2.7) summarize these processes.

$$\begin{aligned}
2\nu\beta^+\beta^+ : & & (Z, A) &\to (Z-2, A) + 2\nu_e + 2e^+, & (2.5)\\
2\nu\beta^+/EC : & \quad e^- + & (Z, A) &\to (Z-2, A) + 2\nu_e + e^+, & (2.6)\\
2\nu EC/EC : & \quad 2e^- + & (Z, A) &\to (Z-2, A) + 2\nu_e. & (2.7)
\end{aligned}$$

Since LN is conserved in $2\nu\beta\beta$, the decay is allowed within the SM. Nevertheless, $2\nu\beta\beta$ is an extraordinarily rare process. A typical half-life ($T^{2\nu}_{1/2}$) of the process exceeds $\sim 10^{18}$ years and can be calculated as:

$$\left[T^{2\nu}_{1/2}\right]^{-1} = \frac{\Gamma^{2\nu}}{\ln(2)} = \left|M^{2\nu}\right|^2 G^{2\nu}. \tag{2.8}$$

Here, $\Gamma^{2\nu}$ is the decay rate, $G^{2\nu}$ is the phase-space factor, and $M^{2\nu}$ are the nuclear matrix elements (NMEs) of the transition. $M^{2\nu}$ is calculated theoretically and is heavily reliant on the choice of the nuclear model. For example, Interacting Shell Model (ISM) was used in [25] and Quasiparticle Random Phase Approximation (QRPA) in [26]. NMEs of $2\nu\beta\beta$ are discussed in more detail in section 2.4.

Similar to the ordinary β-decay, the energy spectrum of $2\nu\beta\beta$ is continuous with an end-point at the decay's Q-value. A typical shape of the decay spectrum is shown in Figure 2.2. Traditionally, the sum of electron energies (E_{sum}) is plotted on the x-axis.

2.2 Neutrinoless Double Beta Decay

In 1939 Furry proposed existence of a process, which is similar to $2\nu\beta\beta$. The decay known as neutrinoless double beta decay $0\nu\beta\beta$ [27] is also a transition with $|\Delta Z| = 2$,

(a) $2\nu\beta^-\beta^-$

(b) $0\nu\beta^-\beta^-$

Figure 2.3: A simplified scheme of $2\nu\beta^-\beta^-$ and $0\nu\beta^-\beta^-$.

however, without the emission of neutrinos. $0\nu\beta\beta$ is a hypothetical, never before observed, decay which violates the LN conservation and it is forbidden within the SM. Nevertheless, much effort is put towards searching for this rare decay as it has many implications on the knowledge about the opened questions of neutrino physics. If observed, $0\nu\beta\beta$ it would mean that the neutrinos are Majorana particles, as this decay can only occur if this condition is met. The simplest mechanism for this process is the so-called light-neutrino exchange mechanism [28]. A sketch of $0\nu\beta\beta$ is shown in Figure 2.3b.

The possible decay modes of $0\nu\beta\beta$ are described by:

$$0\nu\beta^-\beta^- : \qquad (Z,A) \to (Z+2,A) + 2e^-, \tag{2.9}$$

$$0\nu\beta^+\beta^+ : \qquad (Z,A) \to (Z-2,A) + 2e^+, \tag{2.10}$$

$$0\nu\beta^+/EC : \quad e^- + \quad (Z,A) \to (Z-2,A) + e^+, \tag{2.11}$$

$$0\nu EC/EC : \quad 2e^- + \quad (Z,A) \to (Z-2,A). \tag{2.12}$$

The half-life for $0\nu\beta\beta$ can be calculated as:

$$\left[T^{0\nu}_{1/2}\right]^{-1} = \frac{\Gamma^{0\nu}}{\ln(2)} = \left|\langle m_{\beta\beta}\rangle\right|^2 g_A^4 \left|M^{0\nu}(g_A^{\text{eff}})\right|^2 G^{0\nu}. \tag{2.13}$$

Here, $m_{\beta\beta}$ is the so-called *majorana neutrino mass.* g_A is the unquenched axial-vector coupling constant, which is traditionally obtained from ordinary β-decay to equal $g_A = 1.269$. As noted in [29] the discrepancies in the calculation of model dependent NMEs can be up to factor of 2 to 4. Knowing the exact value of g_A is crucial because it is raised to the fourth power in (2.13). As a result, it significantly influences the calculated half-life value in the equation. Under the light-neutrino mass mechanism:

$$m_{\beta\beta} = \sum_{i=1}^{3} m_i U_{ei}^2. \tag{2.14}$$

Here, U_{ei}^2 are the mixing matrix elements (elements of PMNS matrix). Unlike its two-neutrino counterpart, $0\nu\beta\beta$ half-life is inversely proportional to the square of effective neutrino mass (due to the presence of neutrino propagator). Not only that $0\nu\beta\beta$ can shed light on the nature of neutrinos, it is also valuable for investigation of the absolute mass scale of neutrinos and neutrino mass ordering.

Since no neutrinos are released, all of the decay energy is transformed into the kinetic energy of the electrons. In an ideal detector, a delta peak would be measured at the Q-value. With a realistic detector, the delta peak is smeared by the experimental resolution. This leads to a very clear experimental signature to look for in $0\nu\beta\beta$ experiments – a Gaussian peak in the E_{sum} spectrum centered at the Q-value (see Figure 2.2). There are, however, many experimental challenges in the search for $0\nu\beta\beta$ that keep this process yet to be observed.

2.3 Current Double Beta Decay Experiments

2.3.1 Experimental Parameters and Sensitivity

The relationship between $0\nu\beta\beta$ half-life and $\langle m_{\beta\beta}\rangle$ motivates much of the experimental efforts in the field of DBD experiments. It is of great importance to determine the value of $T^{0\nu}$, ideally for multiple isotopes (as discussed in section 2.4). It turned out that the current generation of detectors are not sensitive enough to measure the exceedingly rare decay. It is one of the reasons that keeps the search for $0\nu\beta\beta$ ongoing and drives the development of ever more advanced technologies to get more sensitive detectors.

Sensitivity ($S^{0\nu}$) to $0\nu\beta\beta$ describes the detector's potential to measure the process. This value can be calculated (or predicted) even in the case when no events are measured – no discovery. It gives the lower bound on the half-life of the decay that the detector can measure.

Due to the exceptionally long half-lives of DBD processes, it is useful to use a first-order Taylor approximation of the exponential law of radioactive decay when calculating $T^{\beta\beta}_{1/2}$ for experiments measuring only several years. As shown in [30, 31], this approach allows the derivation for $T^{\beta\beta}_{1/2}$:

$$T^{\beta\beta}_{1/2} = \ln(2)\frac{N_A}{W}\varepsilon\frac{am_dt}{n_{OS}}. \tag{2.15}$$

The amount of $\beta\beta$ decaying isotope is described by: N_A – the Avogadro's constant; W – molar mass of the isotope; a – the $\beta\beta$ decaying isotope abundance in the observed source, and m_d – mass of the source. t is the duration of the measurement, and n_{OS} is the number of observed signal events (assuming background-less experiment).

One of the biggest challenges of experiments searching for rare decays is the background reduction. Such experiments are typically placed in underground laboratories with high levels of cosmic ray suppression. Passive shielding is installed to further reduce external background. Materials used to build the detectors are chosen to reduce the contamination and radioactivity levels originating from the detector materials themselves. Another possibility to reduce the background is to use sophisticated analyses and software tools to discriminate the background in favour of signal event. Much of the background radiation can be reduced to (almost) zero using the correct combination of the aforementioned approaches. However, an unavoidable source of background radiation for the $0\nu\beta\beta$ search stems from the $2\nu\beta\beta$ decay of the studied isotope itself. Here, due to the signatures of the two decays (see Figure 2.2), it is desirable to have the best possible energy resolution. Furthermore, the choice of $\beta\beta$ decaying isotope is another decision to be made when designing the experiment. Isotopes with high Q-values are preferred. Such condition ensures that the $0\nu\beta\beta$ peak is above the natural background in the energy spectrum. In order to increase the number of decays it is important to have large amounts of the observed isotope. Isotopes with higher abundance or isotopes which can be relatively easily enriched are favored. Lastly, detector efficiency should be increased in order to limit the amount of *missed* decays.

Background and statistical nature of radioactive decay must always be considered when performing analysis of data from $0\nu\beta\beta$ experiment. It is crucial to consider the possibility that the observed events might originate from background rather than the desired signal. Consequently, various statistical approaches need to be employed to address this issue.

In general, DBD experiments experience very low counts in the region of interest (ROI). Thus, in order to calculate $S^{0\nu}$ Poisson statistics needs to be employed. If the decay is not observed, $S^{0\nu}$ is reported instead of $T^{0\nu}_{1/2}$.

As derived and explained in [30, 31], $S^{0\nu}$ for low-count experiments is given by:

$$T^{0\nu}_{1/2} \geq S^{0\nu} = \ln(2)\frac{N_A}{W}\varepsilon\frac{am_d t}{S_{n_\sigma}(\bar{b})}. \tag{2.16}$$

In simple terms, equation (2.16) describes the lower bound on $0\nu\beta\beta$ half-life an experiment reports with a confidence level given by n_σ.

Equation (2.15) encompasses the experimental parameters described above that physicists consider when designing DBD experiments. Optimization of these parameters is crucial to enhance sensitivity and increase the chances to discover $0\nu\beta\beta$.

2.3.2 Overview of Current Experiments and Techniques

The variety of DBD candidate isotopes gave rise to numerous large scale experimental techniques in the field. The various experimental approaches can be categorized into two basic groups:

1. **Homogeneous detectors** - Experiments in which the detector coincides with the source. This is the most common approach to the $0\nu\beta\beta$ detection, and it is

applied in most of the $0\nu\beta\beta$ experiments. For example, current experiments with gas embedded sources include Xenon (^{136}Xe) based Time Projection Chamber experiments, e.g. nEXO [32] or NEXT-100 [33]. Another group based on the liquid scintillators (using ^{130}Te or ^{136}Xe) include experiments SNO+ [34] or KamLAND-Zen [3], which set the lowest (upper) limit on the neutrino mass so far. Another approach is based on a group of high purity germanium (^{76}Ge) crystal detectors, here LEGEND Experiment [2] is designed to reach the sensitivity of the $0\nu\beta\beta$ half-life of 10^{28} years (90% CL) with total exposure of 10 t.yr. This corresponds to the effective Majorana neutrino mass range $\langle m_{\beta\beta} \rangle < 10 - 20$ meV. Finally, experiments exploiting the bolometric technique (using ^{130}Te and ^{100}Mo) involve CUORE [35] or CUPID-Mo [36]. The advantages of this group of experiments is their ability to maximize detection efficiency and have excellent energy resolution. They can reach large masses of a target isotope. The main disadvantages of these experiments are the relatively high unavoidable background and inability to measure particles' trajectories (only their energies). This results in the fact that these types of experiments do not observe the individual electrons, but rather only the energy they deposited in the detector. Thus, a sum of the electron energy spectrum is often reported as the only measurable quantity (see Figure 2.2).

2. **Heterogeneous detectors** - Experiments where the source and detection system are independent of each other. This category includes the SuperNEMO experiment [37] and its predecessors (NEMO-1 [38], NEMO-2 [39] and NEMO-3 [40]). The approach is based on the so-called "tracker-calorimeter" method where not only the energy spectrum (crucial for distinguishing $0\nu\beta\beta$ from $2\nu\beta\beta$) is measured, but also the outgoing particles' trajectories are reconstructed. The main advantages of this approach are the possibility to significantly reduce the background and to study multiple sources, however this comes at the cost of lower energy resolution and isotope mass.

Experiment SuperNEMO is described in more detail in chapter 3. The advantage is the ability to reconstruct the full kinematics of the DBD using the track reconstruction. It can be exploited in the search for exotic physics, or precise spectrum shape studies. The relevant features are summarized in the next sections.

2.4 Double Beta Decay Rate and Spectrum Shape

The ongoing experiments that are currently being developed or have just started their measurement campaigns are often referred to as ”next-generation” experiments. With the advent of these next-generation DBD experiments, as well as recent generation experiments, the feasibility of conducting precise studies on $2\nu\beta\beta$ decays has significantly increased. This can be primarily attributed to measurements with large statistics of $2\nu\beta\beta$, which have been measured using increasingly powerful and accurate detectors (for example the NEMO-3 experiment collected $\sim 5 \times 10^5$ events [41]). There exists a multitude of reasons that necessitate further exploration into $2\nu\beta\beta$ decays, several of which are the focus of this thesis. Firstly, a more refined calculation of the spectral shapes for $2\nu\beta\beta$, done in [4] and [5], provides insights into the determination of g_A^{eff}, a crucial parameter in the search for $0\nu\beta\beta$. Additionally, it enables the prediction of lower backgrounds originating from $2\nu\beta\beta$ that could interfere with $0\nu\beta\beta$ searches.

Moreover, the abundance of measured $2\nu\beta\beta$ events allows for the examination of beyond the Standard Model (BSM) physics. In general, the BSM physics in the context of $2\nu\beta\beta$ involves various scenarios with exotic particles that participate in the decay, replacing the two neutrinos. Notable, examples include the widely discussed massive sterile neutrinos (with masses in the range $10\text{eV} < m_N < 1\text{MeV}$) proposed in [42], as well as diverse possibilities for decays featuring right-handed neutrinos in the absence of sterile neutrino states, as presented in [43].

In each case, the most important experimental signature to distinguish the proposed decay channels is their effect on the shape of the electron energy spectra and the angular distributions.

2.5 Refined Calculation of $2\nu\beta\beta$ Decay Rates

As shown in equation (2.15) and discussed briefly in section 2.1, the half-life of $2\nu\beta\beta$ depends on the precise calculations of NMEs and the knowledge of the value of g_A. The Gamow-Teller nuclear matrix elements, which depend on the lepton energies, are given by:

$$M_{GT}^{K,L} = m_e \sum_n M_n \frac{E_n - (E_i + E_f)/2}{[E_n - (E_i + E_f)/2]^2 - \varepsilon_{K,L}^2}. \tag{2.17}$$

Where M_n describes the transition in the intermediate states between initial and final nuclear state. E_i, E_f and E_n are the energies of states of initial, final and intermediate nuclei, m_e is the electron mass, and $\varepsilon_{K,L}$ is the lepton energy factor:

$$\varepsilon_K = (E_{e2} + E_{\nu 2} - E_{e1} - E_{\nu 1})/2, \tag{2.18}$$

$$\varepsilon_L = (E_{e1} + E_{\nu 2} - E_{e2} - E_{\nu 1})/2. \tag{2.19}$$

Here, E_{e1}, E_{e2} are the electron energies and $E_{\nu 1}, E_{\nu 2}$ are the neutrino energies. Traditionally, $\varepsilon_{K,L}$ is ignored in the standard calculation of $2\nu\beta\beta$ decay rate because it is considered small. Then, NMEs can be approximated as:

$$M_{GT}^{K,L} \simeq M_{GT}^{2\nu} = m_e \sum_n \frac{M_n}{E_n - (E_i + E_f)/2}. \tag{2.20}$$

This approximation allows to calculate the phase-space factors and the NMEs individually and one obtains equation (2.8), with the standard sum energy spectrum as shown in Figure 2.2.

An improved calculation was performed in [4] for the energy dependence and in [5] for the angular dependence. Here, $\varepsilon_{K,L}$ is considered non-negligible and the Taylor expansion about this factor in equation 2.17 is used up to the fourth order:

$$\begin{aligned} M_{GT}^{K,L} &\simeq \sum_n M_n \frac{m_e}{E_n - (E_i + E_f)/2} \times \\ &\times \left(1 + \left(\frac{\varepsilon_{K,L}}{E_n - (E_i + E_f)/2}\right)^2 + \left(\frac{\varepsilon_{K,L}}{E_n - (E_i + E_f)/2}\right)^4 + ...\right). \end{aligned} \quad (2.21)$$

From here, the individual NMEs comprising the Taylor expansion are defined as:

$$\begin{aligned} M_{GT-1}^{2\nu} &\equiv M_{GT}^{2\nu} \\ M_{GT-3}^{2\nu} &= \sum_n M_n \frac{4m_e^3}{[E_n - (E_i + E_f)/2]^3} \\ M_{GT-5}^{2\nu} &= \sum_n M_n \frac{16m_e^5}{[E_n - (E_i + E_f)/2]^5}. \end{aligned} \quad (2.22)$$

Lastly, by introducing variables representing the ratios of the NMEs,

$$\xi_{31}^{2\nu} = \frac{M_{GT-3}^{2\nu}}{M_{GT-1}^{2\nu}}, \xi_{51}^{2\nu} = \frac{M_{GT-5}^{2\nu}}{M_{GT-1}^{2\nu}}, \quad (2.23)$$

one obtains the a more precise formula for the half-life:

$$\begin{aligned} \left[T_{1/2}^{2\nu}\right]^{-1} &= (g_A^{eff})^4 |M_{GT-1}^{2\nu}|^2 \{G_0^{2\nu} + \xi_{31}^{2\nu} G_2^{2\nu} + \\ &+ \frac{1}{3}(\xi_{31}^{2\nu})^2 G_{22}^{2\nu} + \left[\frac{1}{3}(\xi_{31}^{2\nu})^2 + \xi_{51}^{2\nu}\right] G_4^{2\nu}\}. \end{aligned} \quad (2.24)$$

The NMEs and the phase-space factors (G_i, N_i) can be calculated from theory. Thus, equation 2.24 contains two free parameters to be determined: $\xi_{31}^{2\nu}$ and $\xi_{51}^{2\nu}$.

There are two approaches for the description of transition between initial and final state of the $\beta\beta$ decaying nucleus. In the so-called single state dominance (SSD), only the lowest state of the intermediate nucleus $(A, Z \pm 1)$ is considered to contribute to the transition [44]. On the other hand, in the so-called higher state dominance (HSD), many intermediate states are considered [45]. SSD approach is currently preferred as it was supported by data from NEMO-3 [41]. If one considers SSD, parameter $\xi_{51}^{2\nu}$ can be fixed and thus only one free parameter remains: $\xi_{31}^{2\nu}$.

2.5.1 Energy and Angular Distribution

Refined half-life described in equation (2.24) has important implications on the possibilities of the study of $2\nu\beta\beta$ spectrum shape and the determination of the value of g_A^{eff}. A comparison of the contribution to the sum electron energy (described by T_{ee}) spectrum and the single electron energy (described by T_e) of the refined calculation for various values of $\xi_{31}^{2\nu}$ is shown in Figure 2.4 for two isotopes: ^{100}Mo and ^{82}Se. It can be seen that the parameter $\xi_{31}^{2\nu}$ has direct impact on the shape of the spectra. The difference between the spectral shapes is more pronounced in the single electron energy spectra. This is a promising result, especially for SuperNEMO demonstrator which is capable of measuring the individual electrons.

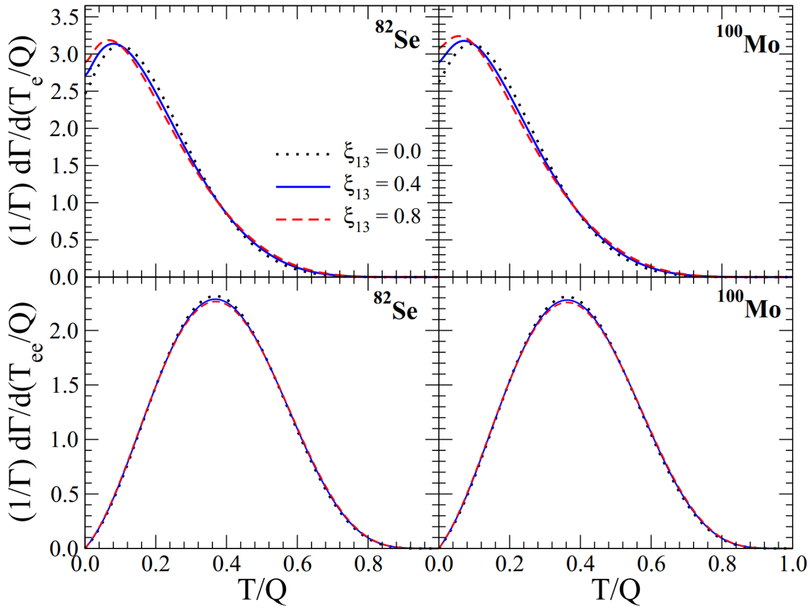

Figure 2.4: Differential decay rates vs kinetic energies normalized by the full decay rate. Spectra are shown for isotopes ^{100}Mo and ^{82}Se. The sum electron energy spectrum (T_{ee}) is shown on the bottom. The single electron energy spectrum (T_e) is shown on top. Spectra are shown for three values of $\xi_{31}^{2\nu}$ parameter. From [4].

Angular distribution is another observable which allows the determination of $\xi_{31}^{2\nu}$. As shown in [5], the differential rate as a function of the angle between the emitted electrons in $2\nu\beta\beta$ (denoted as θ), is given by:

$$\frac{d\Gamma^{2\nu}}{d(\cos\theta)} \propto 1 + K^{2\nu}(\xi_{31}^{2\nu}, \xi_{51}^{2\nu}) \cos\theta, \tag{2.25}$$

with

$$K^{2\nu}(\xi_{31}^{2\nu}, \xi_{51}^{2\nu}) = -\frac{H_0^{2\nu} + \xi_{31}^{2\nu} H_2^{2\nu} + \frac{5}{9}(\xi_{31}^{2\nu})^2 H_{22}^{2\nu} + (\frac{2}{9}(\xi_{31}^{2\nu})^2 + \xi_{51}^{2\nu}) H_4^{2\nu}}{G_0^{2\nu} + \xi_{31}^{2\nu} G_2^{2\nu} + \frac{1}{3}(\xi_{31}^{2\nu})^2 G_{22}^{2\nu} + (\frac{1}{3}(\xi_{31}^{2\nu})^2 + \xi_{51}^{2\nu}) G_4^{2\nu}}. \tag{2.26}$$

Thus, by studying the angular distribution of the measured $2\nu\beta\beta$ events, it is possible to determine the parameter $\xi_{31}^{2\nu}$, which is one of the main aims of this thesis.

2.6 $2\nu\beta\beta$ Beyond the Standard Model

2.6.1 $2\nu\beta\beta$ with Right-Handed Currents

Within the SM, double beta decay is a transition described by a second-order perturbation theory with weak left-handed V-A currents involved. An extension involving also the right-handed V+A currents is presented in [6]. The effective Lagrangian using both the left-handed and right-handed currents is described by:

$$\begin{aligned}\mathcal{L}_M &= \frac{G_F \cos\theta_C}{\sqrt{2}}\left[(1+\delta_{SM}+\epsilon_{LL})j_L^{\mu}J_{L\mu} + \epsilon_{RL}j_L^{\mu}J_{R\mu} + \right. \\ &+ \left. \epsilon_{LR}j_R^{\mu}J_{L\mu} + \epsilon_{RR}j_R^{\mu}J_{R\mu}\right] + h.c. \end{aligned} \tag{2.27}$$

Where G_F is the Fermi constant which governs the strength of the currents involved, θ_C is the Cabbibo angle. j_X^{μ} and $J_{X\mu}$ with $x \in (L, R)$ are the leptonic and hadronic currents respectively. δ_{SM} encodes the SM electroweak radiative corrections and ϵ_{XY} encapsulates the new physics. The latter terms in equation (2.27) are of particular interest for this project: ϵ_{LR} and ϵ_{RR}, which represent the RH leptonic currents:

$$j_R^{\mu} = \bar{e}\gamma^{\mu}(1+\gamma_5)\nu. \tag{2.28}$$

Here, ν is a four-spinor field of the light neutrino. Neutrino could be either Dirac ($\nu = \nu_L + \nu_R$) or Majorana ($\nu = \nu_L + \nu_L^C$) in nature, without affecting the calculations. In conjuction with LN violation it could be of crucial interest for the experiments searching for $0\nu\beta\beta$. If ν is of Majorana nature then terms with ϵ_{RL} and ϵ_{RR} will violate LN and give rise to contributions for $0\nu\beta\beta$ [46]. However, if the neutrino in equation (2.27) is of Dirac nature, there exists a possibility for a LN non-violation, as presented in the left-right symmetric models [47]. In such case, if the RH currents were observed and the LN violation was not observed, it would exclude the possibility of $0\nu\beta\beta$ existence, as the neutrinos would be strongly suggested as Dirac particles.

The involvement of RH currents, either exchanging one neutrino or both, alongside with the SM $2\nu\beta\beta$ is presented in Feynman diagrams in Figure 2.5.

To obtain the full differential decay rate, a coherent sum over the Feynman diagrams is performed and the amplitude of $2\nu\beta\beta$ is obtained. The results are presented in [6] with the details of the calculation provided in supplemental material [48]:

$$\frac{d\Gamma^{2\nu}}{dE_1 dE_2 d\cos\theta} = \frac{\Gamma^{2\nu}}{2}\frac{d\Gamma^{2\nu}_{norm}}{dE_1 dE_2}[1 + \kappa^{2\nu}(E_1, E_2, \epsilon_{XR})\cos\theta]. \tag{2.29}$$

Where, $\kappa^{2\nu}(E_1, E_2)$ is an angular correlation factor dependent on the lepton energies. Figure 2.6 shows the difference between the SM and the RH currents involving normalized spectra for T_e and T_{ee} for the isotope of ^{82}Se.

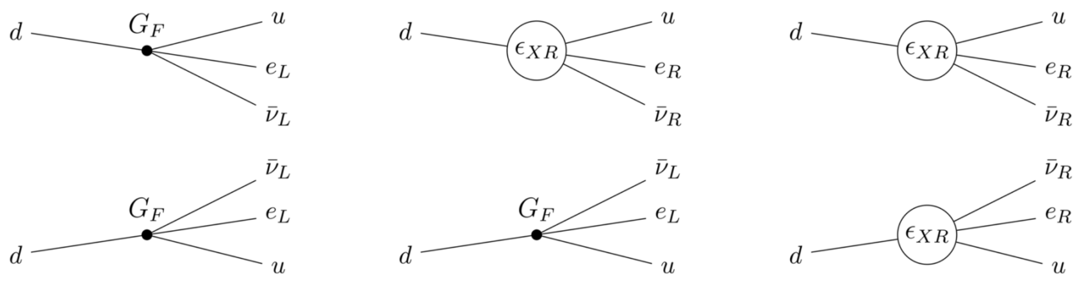

Figure 2.5: From left to right: Feynman diagram of the SM $2\nu\beta\beta$ with the strength given by Fermi constant G_F; transition involving one RH interaction with strength $\epsilon_{XR}G_F$; transition involving two RH interactions. From [6].

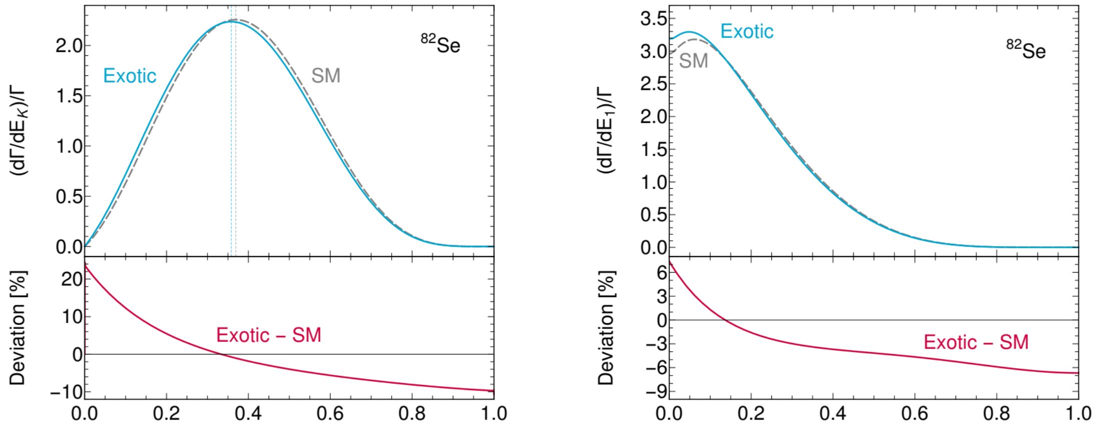

Figure 2.6: Comparison of the sum energy spectra (left) and single energy spectra (right) for the SM and RH involving $2\nu\beta\beta$ for the isotope of ^{82} Se. From the supplemental material of [48].

Integrating over the electron energies, one obtains an angular distribution in the form similar to (2.25):

$$\frac{d\Gamma^{2\nu}}{d(\cos\theta)} = \frac{\Gamma^{2\nu}(\epsilon_{XR})}{2}(1 + K^{2\nu}(\epsilon_{XR})\cos\theta) \tag{2.30}$$

Here, $\Gamma^{2\nu}$ is the total decay rate consisting of the SM and RH parts, it can be approximated as:

$$\Gamma^{2\nu}_{Se} \approx \Gamma^{2\nu}_{SM}(1 + 6.07\epsilon^2_{XR}), \tag{2.31}$$

On the other hand, the angular correlation factor is approximated as:

$$K^{2\nu}_{Se} \approx -0.64 + 6.2\epsilon^2_{XR}. \tag{2.32}$$

The relationship between $K^{2\nu}$ and ϵ_{XR} is depicted in Figure 2.7.

The primary distinction between the SM and the RH currents lies in the preferred direction of electron emission. In the SM, two electrons are predominantly emitted in opposite directions (back to back) with $K^{2\nu} < 0$. Conversely, in the RH currents, two

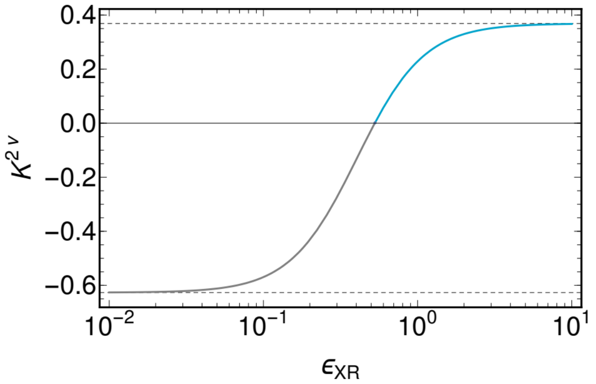

Figure 2.7: Relationship between $K^{2\nu}$ and ϵ_{XR} for the isotope of ^{100} Mo. From the supplemental material of [48].

electrons are predominantly emitted in the forward direction with $K^{2\nu} > 0$. This is known as the forward-backward asymmetry ($A_\theta^{2\nu}$) and it is a clear signature to look for when searching for RH currents. One can determine the ratio between the number N of forward electrons $\theta < \pi/2$ and the backward facing electrons $\theta > \pi/2$:

$$A_\theta^{2\nu} = \frac{N_{\theta>\pi/2} - N_{\theta<\pi/2}}{N_{\theta>\pi/2} + N_{\theta>\pi/2}} = \frac{1}{2}K^{2\nu}. \tag{2.33}$$

Search for RH currents in terms of single electron energy spectra and angular distributions can be probed by experiments with access to the full decay's kinematics.

2.6.2 $2\nu\beta\beta$ with Sterile Neutrinos

In [7] authors suggest existence of another mode of DBD, where one of the active neutrinos is exchanged by a sterile neutrino N. The effective Lagrangian is given by:

$$\begin{aligned} \mathcal{L}_M &= \frac{G_F \cos\theta_C}{\sqrt{2}} \Big[(1+\delta_{SM}) j_L^\mu J_{L\mu} + \\ &+ V_{eN} j_L^{N\mu} J_{L\mu} + \epsilon_{LR} j_R^{N\mu} J_{L\mu} + \epsilon_{RR} j_R^{N\mu} J_{R\mu}\Big] + h.c. \end{aligned} \tag{2.34}$$

With the strength of the mixing between the active and sterile neutrino given by V_{eN}. V_{eN} is dependent on the sterile neutrino mass m_N. Double beta decay with a sterile neutrino would be possible in the mass range $m_N < Q_{\beta\beta} <$ few MeV. Since V_{eN} is dependent on m_N, the change in measured spectrum is affected by m_N as well, mainly by shrinking the endpoint due to non-negligible values of m_N.

CHAPTER 3

SUPERNEMO EXPERIMENT

The SuperNEMO Experiment represents a next-generation detector designed to search for variety of DBD channels. While the primary goal is the investigation of $0\nu\beta\beta$, it also serves as a state-of-the-art instrument for precision analysis of $2\nu\beta\beta$, as successfully demonstrated by its precursor, the NEMO-3 experiment. Situated within the Modane Underground Laboratory (Laboratoire Souterrain de Modane - LSM), the first module, the Demonstrator, contains 6.11 kg of enriched ^{82}Se as the DBD decaying isotope. The selenium is installed in form of thin foils within the center of the detector. In contrast to the cylindrical shape of the NEMO-3 detector, SuperNEMO adopts a planar geometry (see Figure 3.1). The size of the Demonstrator is approximately $6 \times 4 \times 2\ m^3$. With the experience from the predecessor experiments, a number of additional design changes were introduced so to reduce the expected background levels, increase detection efficiency and improve energy resolution.

The complex design of the SuperNEMO Demonstrator comprises of four primary components: 1) the DBD source foil, 2) the particle tracking detector, 3) the segmented calorimeter, and 4) the passive shielding. These elements form the foundation of the tracker-calorimeter technology, which are described in more detail in the following text. An example of a DBD event traversing the individual parts of SuperNEMO is depicted in Figure 3.2.

3.1 Detector Design

3.1.1 DBD Source Foils

The tracker-calorimeter design employed in the NEMO-3 experiment showcased the advantages of utilizing multiple isotopes as sources for DBD. Extensive R&D efforts were carried out to investigate various candidate isotopes [49], including ^{82}Se, ^{48}Ca,

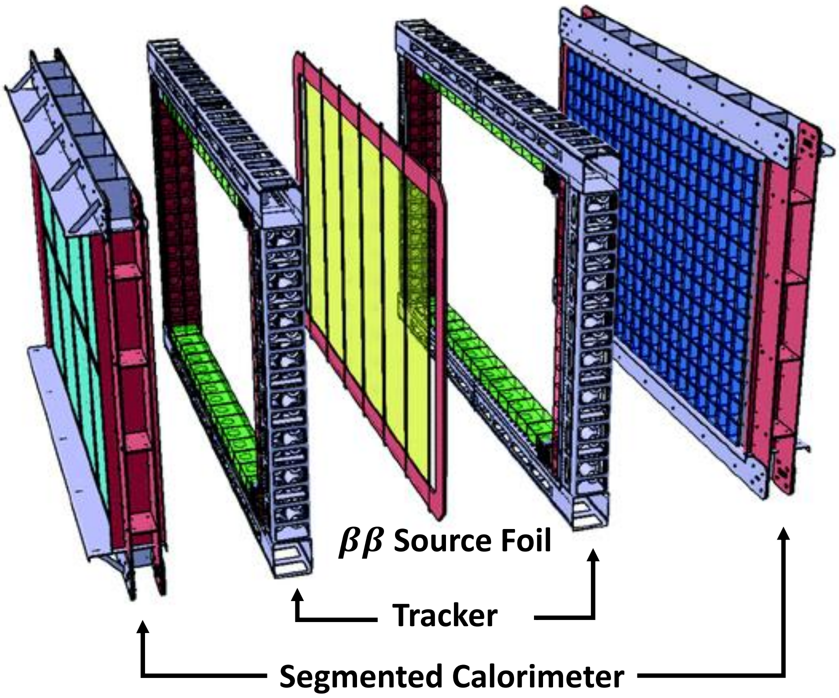

Figure 3.1: A schematic view of the SuperNEMO Demonstrator with the individual components indicated.

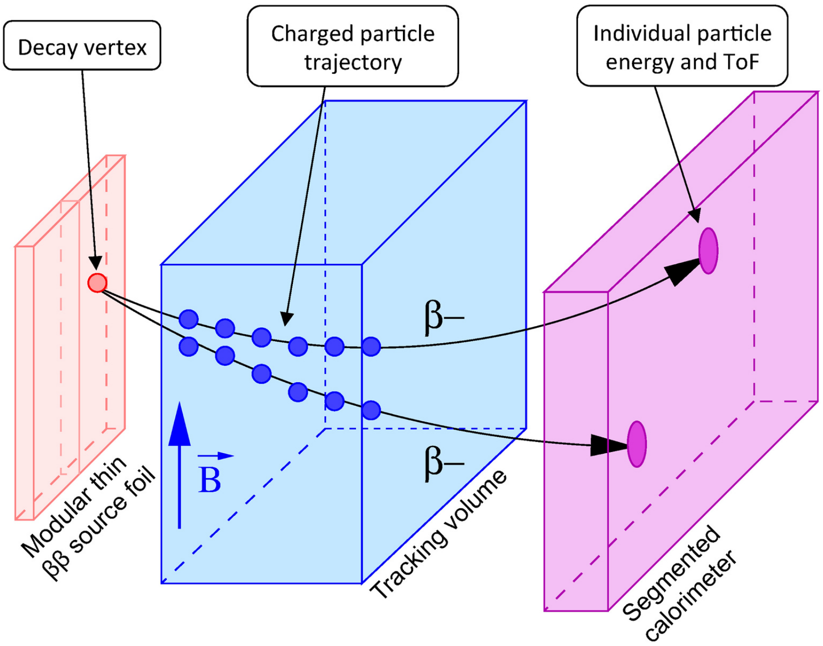

Figure 3.2: Schematic representation of detection principle of SuperNEMO demonstrator.

and ^{150}Nd. In principle, any DBD candidate isotope could be chosen as long as it can be manufactured in the form of thin foils. Ultimately, ^{82}Se was selected as the source isotope for the SuperNEMO Demonstrator due to its high Q-value and the possibility to enrich ^{82}Se to almost 100%. The Q-value for ^{82}Se is 2996 keV, while the highest γ-line of one of the common background contributors, ^{208}Tl, is at 2615 keV.

The Demonstrator comprises a total of 34 selenium foils, each measuring 0.3 mm in thickness. The total mass of the source foil is 6.25 kg (^{82}Se accounts for 6.11 kg). The improved preparation methods described in [50], which were employed in the production of the source foils, ensure that the foils are highly radio-pure. To achieve a foil thickness ranging from 40 to 55 mg/cm^2, powdered selenium was deposited onto thin mylar strips. Upon the installation in the detector, precise laser measurements of the foil geometry were conducted, with an accuracy of 10 μm. These measurements revealed bending of the source foils in certain areas. The realistic source foil geometry is accounted for in the simulation software.

3.1.2 Tracker

The flagship technology of the SuperNEMO detector is the particle tracker. In order to reconstruct the trajectories of charged particles, a system of 2034 tracker cells – detectors run in Geiger mode – consisting of a central anode at around (1600 ± 50) keV surrounded by 12 field shaping wires (shared among cells) envelope the source foil. A schematic view of the tracker cell is shown in Figure 3.3. These cells form the basis of the tracking technology. The tracker is composed of a series of drift-cells, each containing an anode wire, with a diameter of 50 μm surrounded by 12 grounded field-forming wires of diameter 40 μm, which are shared among the neighbouring cells. The length of the wires is ~ 3 m. Cathode caps are placed at each end of the cells. Together, there are 9 rows of cells on each side of the source foil placed in 113 columns. This amounts to a total of 2034 drift cells. The gas mixture used inside the tracker is composed of 95% of Helium, 4% of Ethanol, and 1% of Argon. A slight over-pressure is maintained inside of the tracker at all times so as to maintain a flow of radon-cleaned air which passes through the anti-radon facility dedicated to decreasing radon concentration.

To determine the three-dimensional trajectory of a charged particle interacting within the wire chamber, two quantities are measured by each cell. The interaction distance, denoted as r, is obtained by collecting the charge on the anode wire. Meanwhile, the interaction height, denoted as z, is determined by measuring the time difference in plasma propagation between the two cathodes. By combining these two data points obtained from each triggered cell as the particle traverses the tracking volume, the complete trajectory of the particle can be reconstructed.

The tracker provides the possibility to identify individual electrons in a DBD

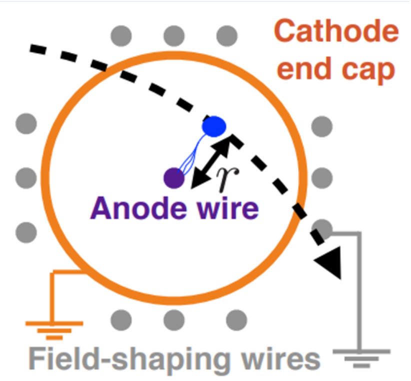

(a) Top view.

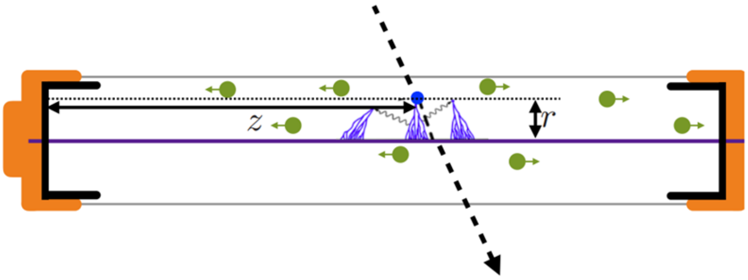

(b) Side view.

Figure 3.3: A schematic view from top and side of the SuperNEMO's Geiger cell.

event, thereby enabling the extraction of single-electron energy spectra and angular distributions. The position of the decay vertex can be determined by extrapolating the reconstructed particle track to the source foil. Additionally, the particle's charge and species can be determined by analyzing the radius and length of the trajectory in presence of a magnetic field. The magnetic field is generated using a solenoid coil, which surrounds the detector. The magnetic field generated within the coil is approximately 25 Gauss. At the moment of writing this text, the decision to turn on the magnetic field has not been taken. The reason is that once the magnetic field is turned on, parts of the detector will be permanently magnetized. The experience with NEMO-3 have shown that the homogeneity of the magnetic field is difficult to achieve. This makes the track reconstruction more difficult. Once the detector is magnetized it is not reasonable to turn it off. It is planned that at least the first few physics data-taking runs will be without the magnetic field on. Particle identification, facilitated by the tracker, serves as an excellent tool for rejecting background events.

3.1.3 Calorimeter

The energy deposited by charged particles in the detector is measured using segmented calorimeter walls. These walls, located on each of the six sides of the detector, consist of plastic scintillators coupled to photomultiplier tubes (PMTs) known as optical modules

(OMs). There are a total of 712 OMs, each with different properties based on their installation side, composition, and purpose.

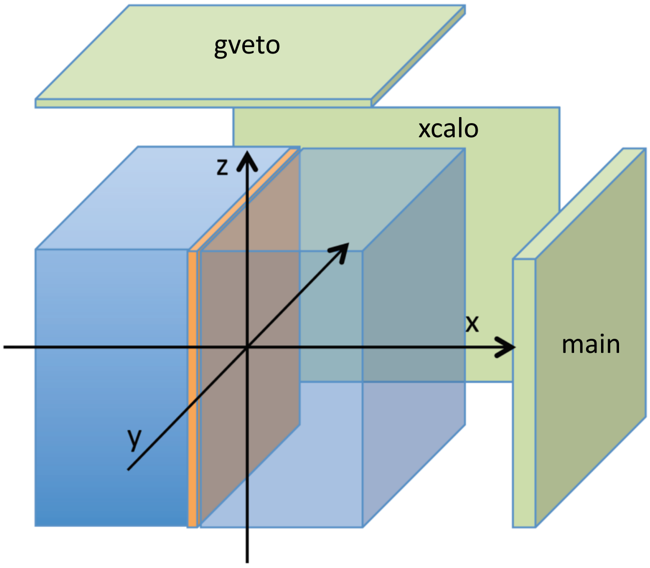

(a) Scheme of the SuperNEMO calorimeter walls. The coordinate system is depicted as well.

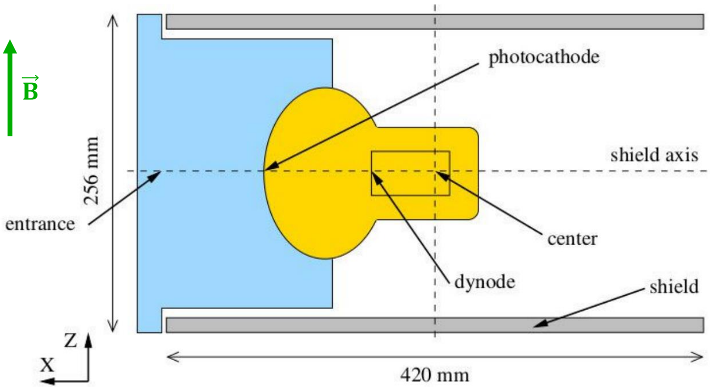

(b) Scheme of the Main wall Optical Module.

Figure 3.4: Segmented calorimeter geometry and dimensions.

The calorimeter is divided into three parts: the main wall, xcalo, and gveto. Figure 3.4a illustrates the placement of these parts within the detector's geometry and also depicts the coordinate system used in this thesis. The two main walls, which have the most OMs (520), contain scintillators that provide the best energy resolution (approximately 8% at 1 MeV [51]). These scintillators were manufactured by NUVIA CZ, a Czech company. They are made of polystyrene with added wavelength shifters pTP (0.6%) and POPOP (0.05%). The R&D process for these scintillators is described in [52]. Each block of plastic scintillator has dimensions of $256 \times 256 \times 141\text{mm}^3$ and is coupled to an 8-inch PMT from Hamamatsu company. The time-of-flight measurements are supported by the time resolution of the OMs of < 400 ps.

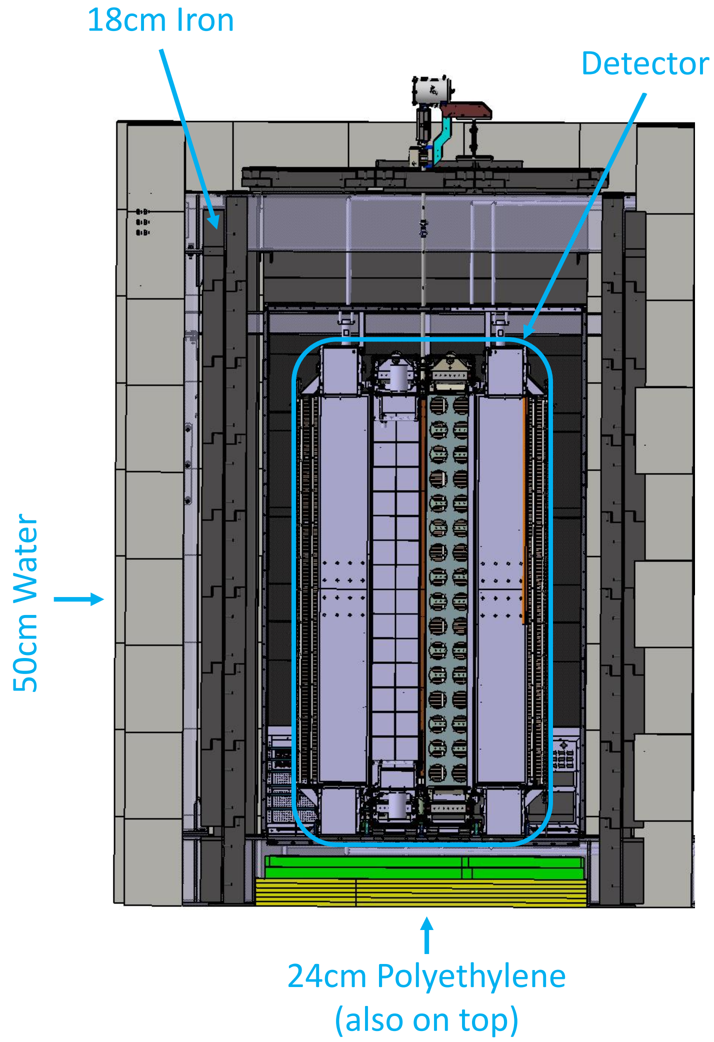

Figure 3.5: Cross section view (in the xz-plane) of the SuperNEMO Demonstrator. The individual passive shielding layers are identified. The polyethylene layers are both on bottom and top of the detector, which is not depicted in the scheme.

The xcalo and gveto walls consist of 128 OMs and 64 OMs, respectively, with energy resolutions of $\sim$ 12% and $\sim$ 15% at 1 MeV. Calibration of the calorimeter is ensured by the automatic system which employs a set of 42 ^{207}Bi sources. These are installed above the detector and can be automatically lowered inside for calibration measurements.

3.1.4 Shielding

SuperNEMO´s goal is to reach zero background in ROI of $0\nu\beta\beta$ during the measurement period. The natural background radiation from cosmic muons is suppressed by a factor of $\sim 10^6$. This is given by the fact that SuperNEMO is placed within the deepest (European) laboratory, with depth of $\sim$ 1.7 km, which equals to 4800 m.w.e. Nevertheless, as SuperNEMO aims to study rare processes, additional layers of shielding

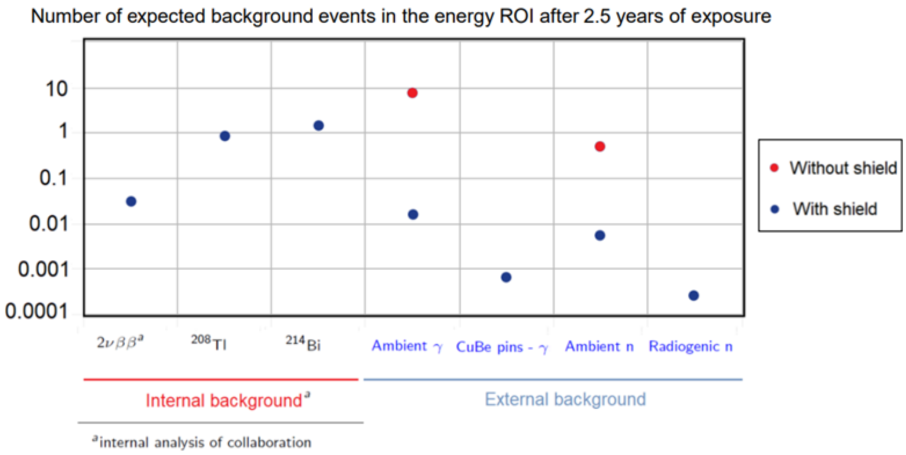

Figure 3.6: Expected background counts from various sources for 2.5 years of measurement, within $0\nu\beta\beta$ ROI. From [10].

are desired to reduce the amount of external background. A detailed study of the possible materials and geometries to be used to shield against external radiation was performed in [10]. To shield from gamma radiation, an 18 cm thick layer of iron is planned to be installed by the end of 2023. Second, to shield from neutrons, a combination of Polyethylene and water is proposed. Containers filled with water, with a total thickness of 50 cm, will be installed around the detector, whereas a 24 cm layer of Polyethylene will be placed on the bottom and top of the detector. In addition to the layers of passive shielding, to reduce the radon contamination in the air, an anti-radon facility is installed which continuously captures radon from air and flushes the detector. Altogether, the proposed shielding will reduce the flux of gammas by factor of 10, and the flux of neutrons by 2-3 orders of magnitude.

The internal background for $0\nu\beta\beta$ stems from two sources. The first, inevitable background arises from the $2\nu\beta\beta$ events within the source foil. Second, main contributions to the internal background come from the contamination of the source foil material, these are mainly the isotopes of ^{208}Tl and ^{214}Bi. The expected background counts are shown in Figure 3.6, the decay schemes for the two isotopes mentioned are shown in Figure 3.7.

3.2 Simulation Software - Falaise

The NEMO collaboration has developed a dedicated multipurpose simulation and data processing software called Falaise, which is based on the widely used Geant4 software developed by CERN [53]. Falaise incorporates essential information about the detector, including its geometry, materials, and physical properties. It also includes a basic track reconstruction algorithm, with advanced algorithms being currently developed.

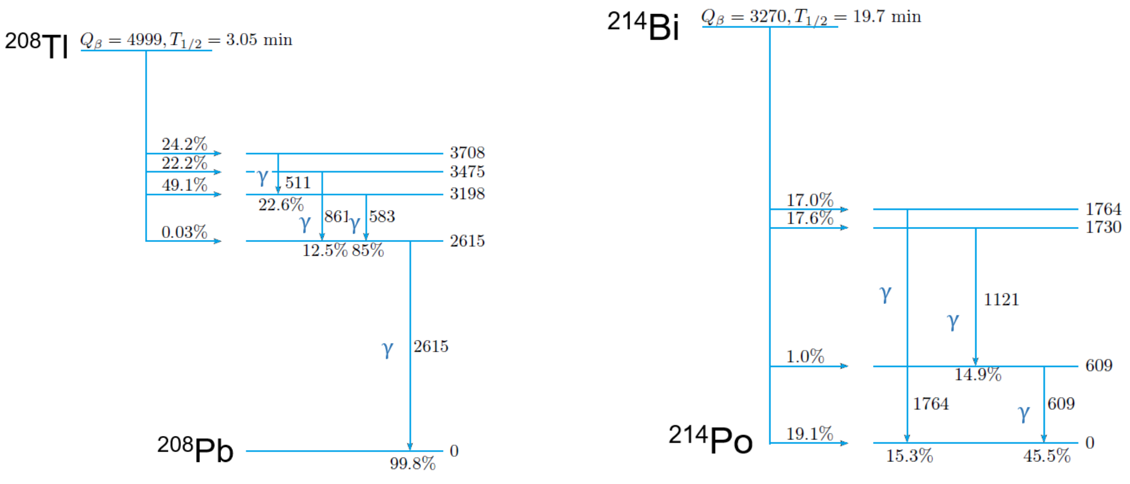

(a) ^{208}Tl (b) ^{214}Bi

Figure 3.7: ^{208}Tl and ^{214}Bi decay schemes showing the strongest gamma transitions. From [10].

A three step approach in simulation of events is used. In the first step, an application called *flsimulate* simulates the passage of particles through a detector. Geant4 is utilized to sample the initial conditions (vertex position, direction, etc.) of the simulated process and calculate relevant information about the particles as they traverse the detector. The simulated data (SD) bank stores various information, such as particle type, kinetic energy, and individual steps within the simulation. Various processes can be simulated, natively implemented via the Decay0 event generator [54], are for example $2\nu\beta\beta$ and $0\nu\beta\beta$ decays of ^{82}Se, ^{214}Bi, and ^{208}Tl. Subsequently within *Falaise*, the user can also chose a settings option for decay vertices (e.g. decays within the source foil volume). Custom processes can be simulated using an input file containing momentum vectors of the simulated particles. The output of *flsimulate* is an SD bank stored in the format developed by collaboration called .brio data format, which contains the desired simulated data.

Although *flsimulate* provides simulated truth data as observed by an ideal detector, studying the data as it would be seen by a *real* detector is generally more useful. To accomplish this, the second step of the simulation process involves the *flreconstruct* application. As the name suggests, the application provides a framework to obtain *reconstructed* data. Falaise includes a mock calibration that mimics the finite resolution of the calorimeter. Particle tracks, from the radii of the triggered Geiger cells, are reconstructed at this stage as well. The input to *flreconstruct* is the SD bank, which is processed through the reconstruction pipeline. The output of *flreconstruct* is another .brio file that contains the Calibrated Data (CD) bank, the Particle Track Data (PTD) bank, and the original SD bank.

Finally, the third step involves converting the .brio files into a format that can be analyzed using common software. Modules within the collaboration have been developed for converting .brio files to ROOT files [55]. In this thesis, the MiModule [56] has been utilized for this purpose.

Additionally, the *flvisualize* application can be employed to visualize the simulated processes. Figure 3.9 illustrates an example of a simulated $0\nu\beta\beta$ event.

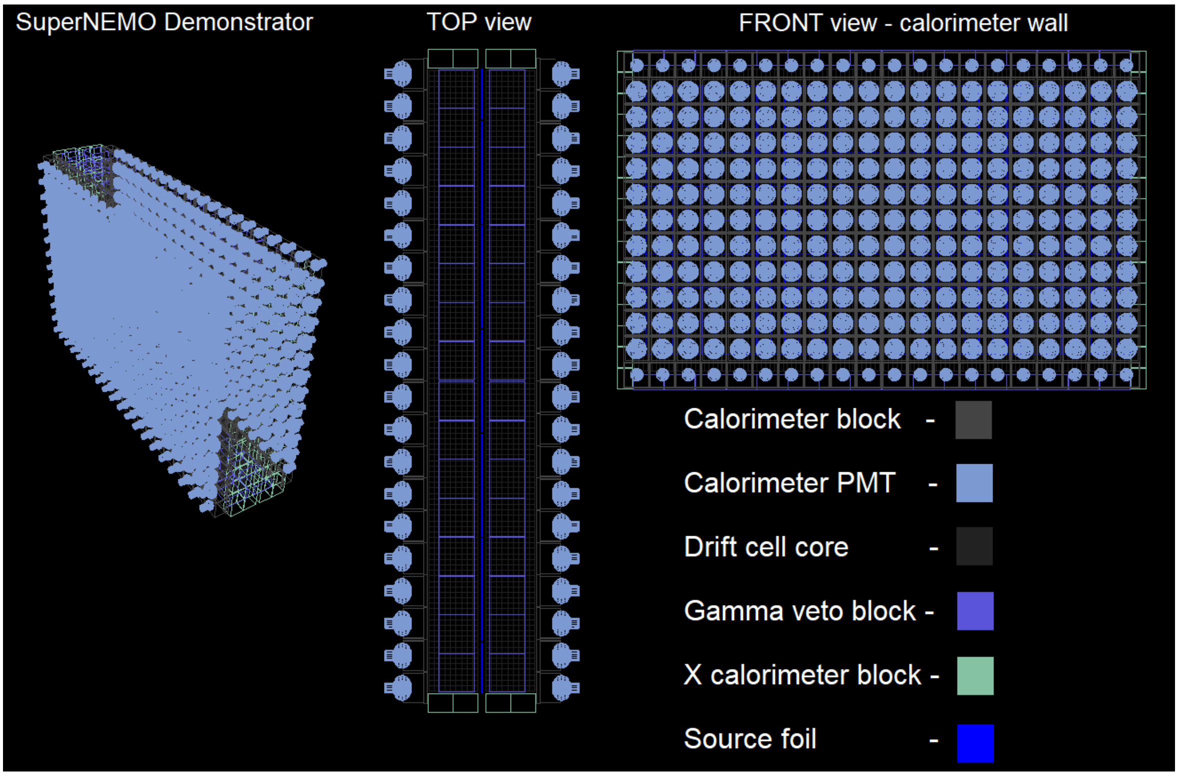

Figure 3.8: Scheme of the SuperNEMO detector as visualized in the *flvisualize* application.

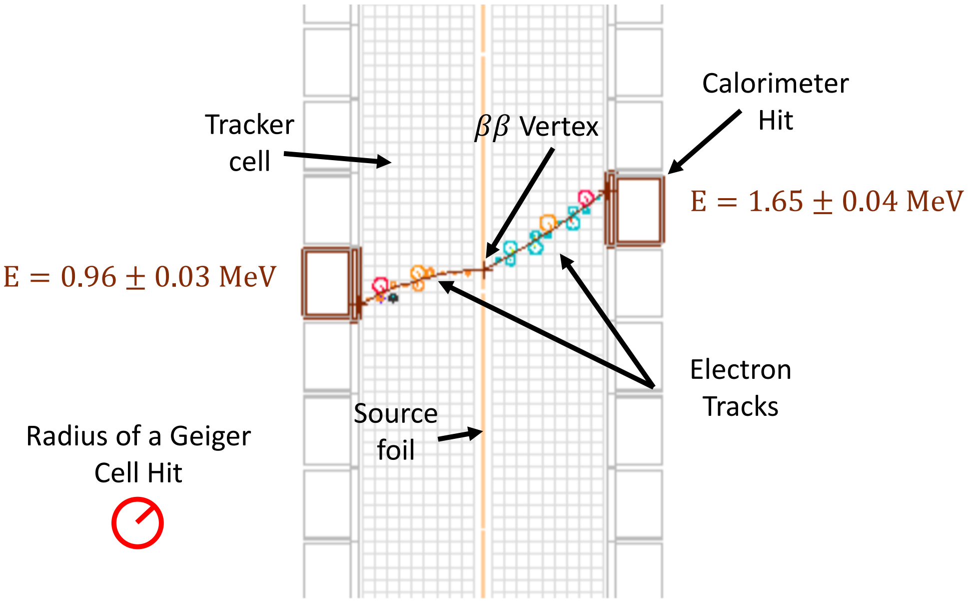

Figure 3.9: An example of simulated $0\nu\beta\beta$ event. The energy deposited by the electrons is marked in the image. The *circles* represent the radii of the triggered Geiger cells (see section 3.1.2).

CHAPTER 4

GOALS OF DOCTORAL THESIS

The subject of this project is the study of new physics which can be probed by the SuperNEMO experiment. The main objectives can be summarized as follows:

1. **Experimental tasks**:
    (a) The construction of the SuperNEMO Experiment has entered its last phase. I have taken part in the construction campaign dealing with gas tightness, which was one of the challenges in the construction of the detector.
    (b) The data-taking runs are soon to begin and as a part of the procedure, the so-called *data-taking shifts* are planned. Each member of the collaboration, myself included, is expected to take part in these *shifts*.
2. **Software tasks**:
    (a) The main simulation and analysis tool used in the collaboration is the Falaise software. As part of my contributions, **I've designed** a small software library. This library is capable of transforming theoretical input spectra into appropriate formats for Falaise. This is achieved through the process of sampling momentum vectors. One of my objectives involves integrating this sampling framework into Falaise, allowing other team members to utilize it effectively.
3. **Analysis tasks:**
    (a) Study of the detector's response to angle measurements between electrons is one of key tasks. Here, I intend to evaluate the relationship between decay and escape angles (as defined in chapter 5). **Furthermore, I have developed a framework** – and described it in this thesis – **which calculates the detector response function.** The future activities will include the

attempts at unfolding the angular distribution, testing of various simulation configurations and processes and the implementation of the new tracking algorithm that is being developed for SuperNEMO.

(b) Study of new physics. The initial task, before fitting the measured spectra is to assess the feasibility of SuperNEMO as tool to observe subtle changes in the predicted distributions. **This is task is completed and summarized in chapter 6.** A short outline of the fitting procedure is provided at the end of this chapter and will be one of the main goals in the future.

CHAPTER 5

STUDY OF ANGLES

In chapter 2, several potential new physics mechanisms involving DBD processes were discussed. These mechanisms are best investigated by analyzing the shapes of the single-electron energy spectra and angular distributions, with the latter being theoretically more sensitive in some cases. However, in most of the cases, experiments can only measure the sum of electron energies and cannot distinguish between individual electrons. There are exceptions to this limitation, notably the NEMO-3 experiment and its successor, SuperNEMO, described in chapter 3. These experiments offer access to complete decay kinematics, enabling the measurement of individual electron tracks. This is a unique feature in the field of DBD.

Originally, The NEMO-3 experiment served as a pioneering detector that demonstrated the potential of combining tracking and calorimetry technologies in DBD measurements. Among its significant contributions, one study examined two competeing hypotheses, namely the Single State Dominance (SSD) and the Higher State Dominance (HSD) hypotheses, which impact the shape of measured spectra [41]. This study highlighted the substantial advantage of having access to both single-electron energy spectra and angular distributions in exploration of new physics to distinguish between hypotheses. In order to confidently exclude the HSD hypothesis, the study focused on analysis of the single-electron energy spectra.

The angular distribution was also a subject of study, but unresolved disparities between the simulated and the measured data were observed. Figure 5.1 depicts the comparison between the MC simulation and measured data of the angular distribution (here represented by $cos\Theta$). Several noteworthy observations arise from this figure. First, the experiment measured an unprecedented amount of statistics, approximately 5×10^5 events, demonstrating the viability of precision physics through statistical analysis with such detector design. Second, a significant deviation is evident in the plot, particularly notable for electrons around $cos\Theta \approx 0$ and tracks with very small angles

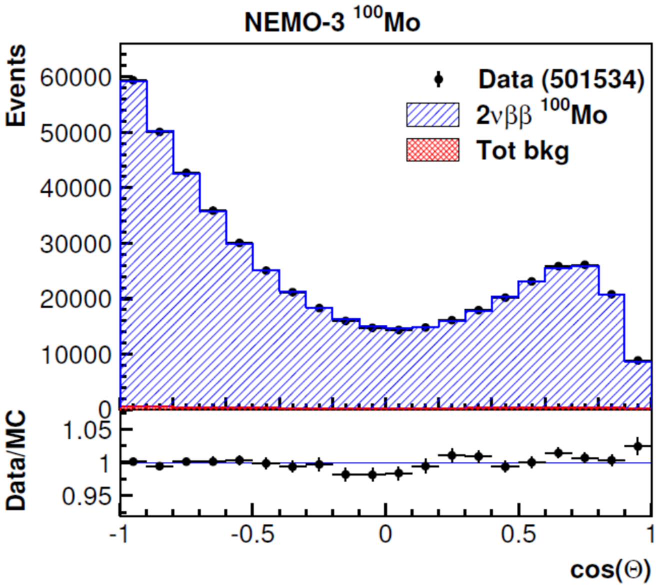

Figure 5.1: NEMO-3 measured angular distribution. The discrepancy between MC simulation and measured data is shown in the bottom figure residual plot. From [41].

between electrons. These discrepancies could potentially originate from various sources. For instance, some factors might not have been accounted for in the simulation.

As this was the pioneering study of such kind, there are still a number of open questions when it comes to understanding how capable such detector technology is in terms of measuring the angle between the electrons through easier track reconstruction conditions.

The SuperNEMO, as the successor technology to the NEMO-3, is expected to expand the potential to use the angular distributions in search for new physics within DBD.

Several potential advantages can be highlighted when one compares SuperNEMO to NEMO-3. For instance, the choice of a simplified planar geometry in SuperNEMO, as opposed to the cylindrical geometry of NEMO-3, is anticipated to simplify the simulations and enhance angle determination between electrons. The efficiency of SuperNEMO is increased in comparison to the NEMO-3, which should in principle increase the total measured statistics, if the amount and the source isotopes were the same for both experiments. The choice of ^{82}Se as a decay source for the SuperNEMO, poses a disadvantage relative to the most represented source ^{100}Mo used in NEMO-3. ^{82}Se has a longer $T_{1/2}$ by roughly one order of magnitude when compared to the ^{100}Mo. This means that one should expect lower amount of decays by roughly one order of magnitude if the experiments differed only by the $T_{1/2}$ of the observed isotope.

Moreover, multiple factors with uncertain impacts on angle measurement quality come into play. For instance, the decision regarding whether (and when) to activate the magnetic field for SuperNEMO was not taken yet. The detector has a magnetic coil installed about the tracker but it was not turned on, yet. It is already known that some of the early data-runs will be recorded without the presence of the magnetic field, reasons for this are discussed in chapter 3. This may decrease particle identification efficiency and, consequently, the efficiency of signal-background discrimination. On the other hand, it will simplify track reconstruction and potentially enhance precision of the angle reconstruction. Additionally, a novel tracking algorithm based on the Legendre transform is under development [57], aiming to provide improved track reconstruction capabilities. These combined advancements position SuperNEMO as a promising platform for enhancing the precision of measuring angles between electrons when compared to its predecessor, NEMO-3.

In the current chapter we attempt to lay groundwork for a detailed analysis of the detector's performance in terms of the angular distribution. The goal, in the future, will be to assess the effects of the magnetic field and the new track reconstruction algorithm on the angular distribution. Section 5.1 follows a similar study done in [30], intending to qualitatively describe the impact of the finite thickness of the source foil on the passage of electrons. It also aims to study the effects of tracker geometry and design on measurements of the so-called escape angle (defined later in section 5.1).

In the section 5.2 we attempt to quantify these effects in terms of the angular correlation. Potential methods for improvements are presented and discussed in section 5.3.

5.1 Detector Effects

In [30], an analysis of the vertex reconstruction was performed on a set of various modes of DBD. Studied data-sets included: $2\nu\beta\beta$, $0\nu\beta\beta$, $0\nu\beta\beta\chi^0$ and $0\nu\beta\beta\chi^0\chi^0$ [1]. As part of the analysis, the angular dependence of the vertex reconstruction precision was studied. A number of qualitative conclusions were drawn about the behavior of the measured angular distribution.

In this work, a similar study is performed which follows the methodology in [30], however, a more general case is investigated. In order to determine the effects of the detector, a data-set following uniform distribution both in terms of energy and angles is generated for the purposes of this study. The data-set is simulated using the *Falaise* software with the default simulation options. These include: the magnetic field being turned on set at the default value of $\sim 25G$; uniform foil thickness and geometry (in reality the source foils are bent); *old* track reconstruction algorithm [2]. The angles are obtained from the scalar product of the momentum vectors obtained in the simulation

---

[1] χ^0 stands for Majoron, a massless Goldstone boson [58]

[2] The *old* reconstruction algorithm refers to the one developed for the NEMO-3 experiment, which is currently implemented in *Falaise*. There are efforts to implement a new track reconstruction under way.

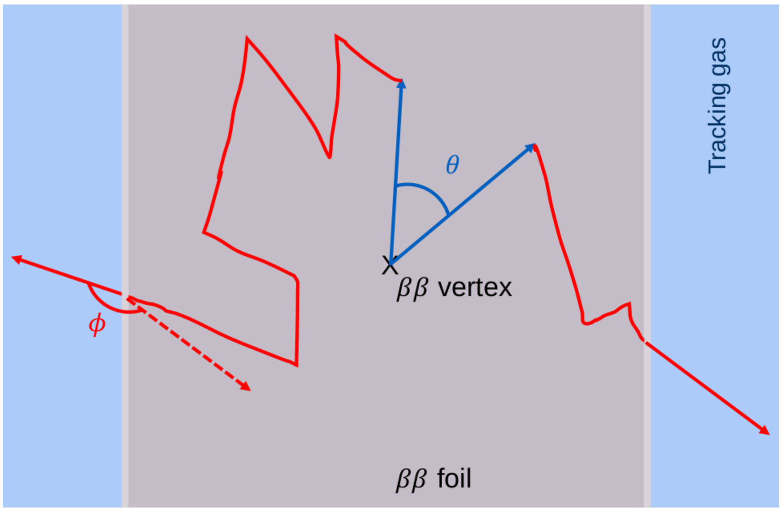

Figure 5.2: A sketch of two electrons that decay with θ traverse through the foil and escape with angle φ. This sketch represents an exxagareted case for illustration purposes.

process. The momentum vector are extracted from the individual simulation steps governed by the Geant4's class G4Step.

It was shown in [30] that due to the finite thickness of the source foil, the angle between the two electrons in DBD at the moment of decay – denoted by θ as the *decay angle* – is not necessarily the same as the angle measured by the detector at the moment, when the electrons escape the source foil and enter the tracker – denoted by φ as the *escape angle* (see Figure 5.2). When the electrons traverse through the source foil, they interact with it in a number of ways that can change their trajectory, i.e. elastic scattering, bremsstrahlung radiation [59]. This change in trajectory may lead to (sometimes dramatic) change in the measured angle between the two electrons. The Figure 5.2 depicts a situation where in a DBD event, the electrons are emitted with an angle θ, however are scattered multiple times within the foil and escape it with a different angle, $\varphi \neq \theta$. It should be emphasised that this effect happens often and that there is a large uncertainty on the φ. Out goal is to assess and work with this uncertainty.

To calculate the two angles, the scalar product of the momentum vectors is calculated:

$$cos(\theta) = \frac{\hat{p_1} \cdot \hat{p_2}}{|\hat{p_1}||\hat{p_2}|}, \tag{5.1}$$

$$cos(\varphi) = \frac{p_1 \cdot p_2}{|p_1||p_2|}. \tag{5.2}$$

Where, $\hat{p_1}$, $\hat{p_2}$, and p_1, p_2 are the electron momenta at the position of decay, and escape [3], respectively.

---

[3] The escape position is determined as the step where the electrons first enter the tracker volume in

In order to study the detector effects in a most general case, 10^8 events with uniform angular (with respect to angle θ) distribution and uniform energy distributions were simulated. This decision is to make sure that each angle is sampled with the same probability and that the input events are equally distributed, thus we do not favour certain events as would be the case, if we studied for example the case of SM DBD which has a preference for back-to-back electrons.

Each simulated event involves two electrons at the start of the simulation, mimicking the DBD process. The electrons were sampled in energy range of $(0 - 3500)$ keV and in angular range of $(0 - 180)^\circ$. Each event begins inside (or on the surface of) the source foil volume. The magnetic field was set to the default value as described in section 3.2. An example of a simulated DBD event, visualized via *flvisualize*, is shown in figure 3.9.

Once the events were simulated in *Falaise*, a series of data-cuts have been applied in order to filter events which mimic the DBD signature in the detector. The data-cuts are as follows:

an event must have

1. two negatively charged particle tracks reconstructed,
2. two vertices on the source foil,
3. sum of reconstructed electron energies within the range: $0\,\text{keV} \leq E_{sum} \leq 3500\,\text{keV}$,
4. two individual OM hits,
5. two associated OM hits.

The detailed justification for these cuts is described in section 4.1.2.1. of [30].

The effects of the data-cuts are shown in figure 5.3.

Two important features can be noticed in the figure. First, the overall number of events has been reduced from 10^8 to $\sim 1.6 \cdot 10^7$ events. The efficiency of the applied data-cuts on the data using the default settings is, therefore, around 16%. Second, the spectrum shape has been changed - from uniform to a spectrum in which larger angles are preferred. This shows, that the data-cuts, without any explicit assumptions on the decay angle, already provide a preference for the larger decay angles.

Once the track of the particles through the detector has been simulated, φ can be extracted and studied. The comparison of θ and φ distributions is shown in Figure 5.4a.

The shape of the φ distribution is significantly different from θ distribution as it is evident from the figure 5.4a. This can be explained in the following way. The underlying principle between the change in shape from θ to φ is due to the fact that

---

the simulation.

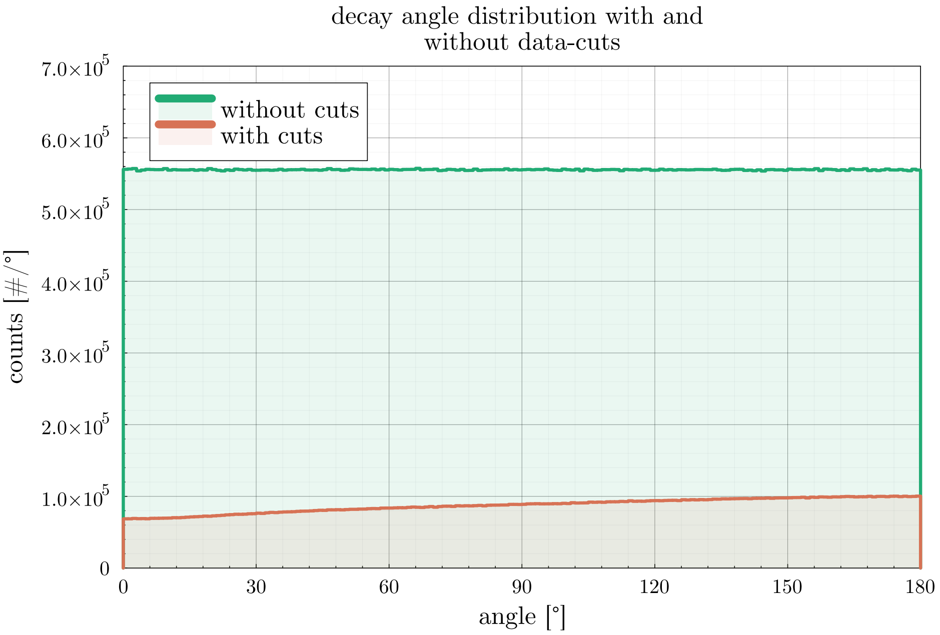

Figure 5.3: The effects of application of the data selection cuts on the decay angle distribution. The data before cuts is shown in green. The effect of applying data-cuts is shown in red.

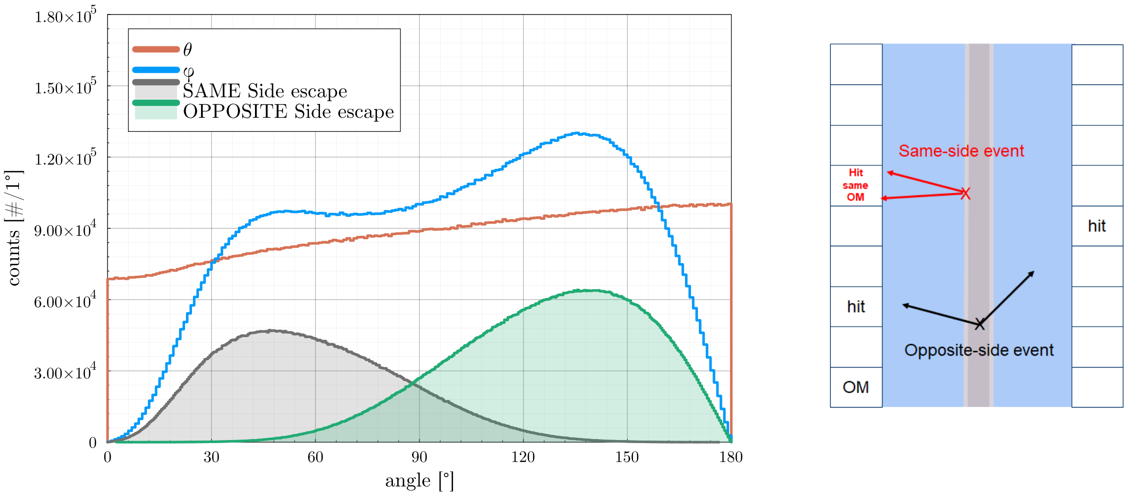

(a) A 1D histogram comparing θ (red) and φ (blue) distributions. The same-side and opposite-side events are depicted as black and green lines, respectively.

(b) Illustration of same-side (red) and opposite-side (black) events.

Figure 5.4: Decay and Escape angular distribution.

an event with θ as the initial decay angle can change into practically *any physical* φ, (i.e. $\varphi \in (0, 180)^\circ$) as the electrons travel through the foil (as sketched in Figure 5.2). However, the probability of this change is not uniform. Secondly, as shown in [30], some configurations are more likely to be successfully reconstructed than others. This effect is seen in both the uniform spectra simulated in this work, and in the various spectra studied in [30]. It appears that the change in distributions $\theta \to \varphi$ is **mostly** governed by the detector geometry (different event acceptance for different event geometries), rather than some effect caused by difference in DBD modes.

The detector's planar geometry suggests a certain symmetry. There is, however, a clear preference for electrons escaping on the opposite sides of the foil – where most events with large escape angles lie – rather than events where the electrons exit on the same side of the foil. This preference is depicted in the figure 5.4a, marked by the black (for the same side events) and the green (for the opposite side events). An illustration of two such events is shown in figure 5.4b.

Normally, due to the symmetry of the detector, two events, one with $\varphi \approx 180^\circ$, the other with $\varphi \approx 0^\circ$ should be identical to each other in terms of track reconstruction as their trajectories are roughly along a single line. This, however, doesn't seem to be the case. A possible reason could be that in an event with very small escape angle, the two electrons could hit the same OM and thus not pass the data-cuts. Overall, it is also more difficult to reconstruct events with smaller angles within the tracking algorithm, since the two tracks are more difficult to distinguish if they are close to each other. This could partially explain the decreased statistics in the lower φ region. On the other hand, this asymmetry can potentially be useful in study of the forward-backward asymmetry of $2\nu\beta\beta$ with RH currents, see section 2.6.

Further qualitative reasons, besides the symmetry, are summarized in the following text. The results are reproduced and referenced from the study made in [30].

There are five features that can be noted in the φ distribution. These are marked in the Figure 5.5. They are split into regions as:

- **Region 1** includes very small escape angles, we call these *closed* angles, roughly $0^\circ \leq \varphi \leq 30^\circ$. Here very few events are present.

- **Region 2** includes intermediate small angles, roughly $30^\circ \leq \varphi \leq 70^\circ$. A bump above the θ distribution line , seen in figure 5.4b, represents an increase in events.

- **Region 3** includes roughly perpendicular events, with a slight decrease of statistics.

- **Region 4** includes intermediate large angles, $110^\circ \leq \varphi \leq 150^\circ$. Here the largest peak in the spectrum is present.

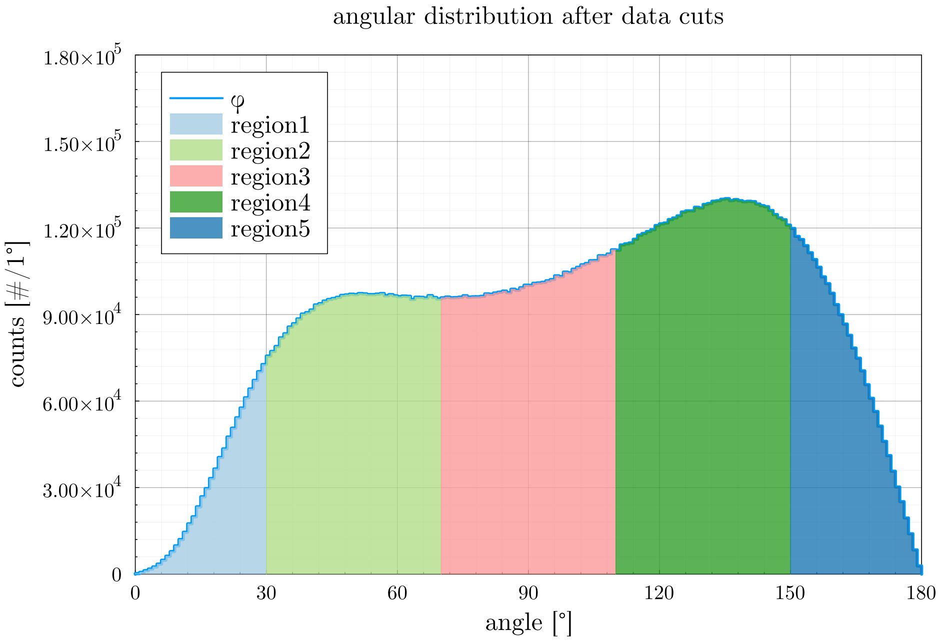

Figure 5.5: A 1D histogram of the φ distribution with the individual regions marked.

- **Region 5** includes very large escape angles, we call these *open* angles, roughly $150° \leq \varphi \leq 180°$. Similar to Region 1 a decrease in number of events is noted.

There are a number of reasons that qualitatively explain the shape of φ.

The decrease in statistics for regions 1 and 5, can be attributed to what we call the opening and closing of the angles.

As noted earlier, an event that starts out with an angle θ can in principle change into any φ (with varying probability), however, an event that has a very small θ has more *room* to shift toward higher angles. That is, when the angle is *closed* it can only *open*. The opposite is true for the situation with large θ events. This leads to events in regions 1 and 5 to be shifted more towards regions 2, 3 and 4. Secondly, we can look at these regions in terms of how well they pass through the applied data-cuts.

An illustration of events from regions 1 and 5 is shown in figure 5.6a. Here, two events with both electrons travelling along the source foil are depicted, in red an event from region 1 and in black an event from region 5. Two more events are depicted with electrons travelling roughly perpendicular to the source foil.

When events have very closed/opened angles, both electrons follow roughly the same path along a line. Thus, if **one** of the electrons escapes in the path along the source foil, **both** will travel along the foil. Tracks along the source foil are very difficult to reconstruct due to the tracker cell design – electrons along the foil will trigger only the first rows of the tracker cells. Furthermore, if the magnetic field if turned on, there is a potential for the electron to bend so much that it will return back to the foil. The first and second data-cut are not fulfilled in such a case. Furthermore, for events from region

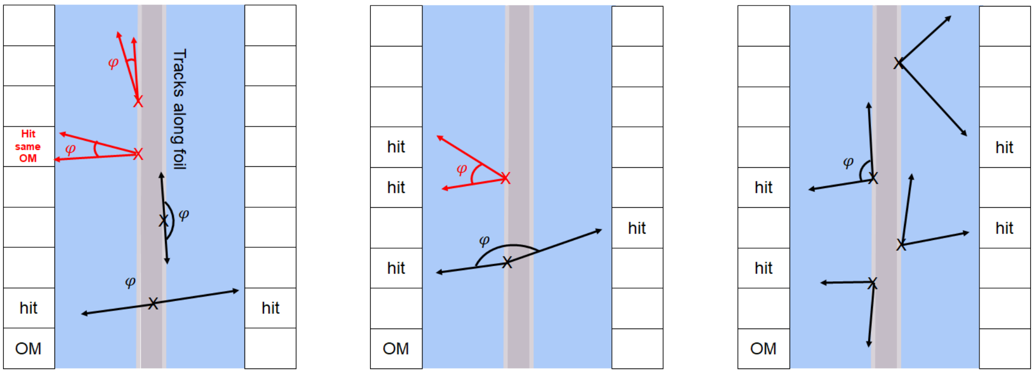

(a) Red: Region 1; black: region 5.

(b) Red: Region 2; black: region 4.

(c) Region 3 events.

Figure 5.6: Examples of events per various regions. The electrons from a DBD are depicted as arrows pointing in the direction in which they escape the source foil (depicted in grey). The tracker is depicted as two blue rectangles, with the OMs shown as white boxes surrounding the tracker. Only the main wall OMs are shown, with hits marked.

1, it is possible that both electrons hit the same Optical Module, thus cuts four and five are not fulfilled. Lastly, electrons with very closed φ will fly along a very similar trajectory, which may be evaluated as a single particle in the reconstruction, rather than two separate electrons. First data-cut is not fulfilled.

The φ distribution shows two rising peaks in the region 2 and region 4. These are regions with events of moderately small/large angles. An illustration of such events is shown in figure 5.6b. Here, two events are shown, both hit two OMs and travelled roughly perpendicular to the source foil. Such events are easily reconstructed. In terms of the shifting of angles from regions 1 and 5, here most events will be shifted into, as it is the next closest (quantitatively described in section 5.2). When one of the electrons escapes the foil perpendicularly – which is the best case scenario for reconstruction, as noted in [30]) – the other electron will likely not be parallel to the foil. These two regions are composed of electrons with *easiest* to reconstruct trajectories and can most easily fulfil all the data-cuts.

The decrease in statistics in the region 3 is explained in [30] and reinforced here. The events with φ close to 90° suffer from the preference of the reconstruction algorithm for events perpendicular to the source foil. When an electron escapes the source foil perpendicularly, the other electron will escape parallel to the foil. Such events are troublesome for vertex reconstruction, due to the large uncertainty in the track reconstruction. In this category, there will always be a trade-off in quality of the reconstruction. The illustration for such events is shown in figure 5.6c. These events suffer from difficulty in passing the second data-cut.

So far, the study reconstructed and supported the findings from [30], while using

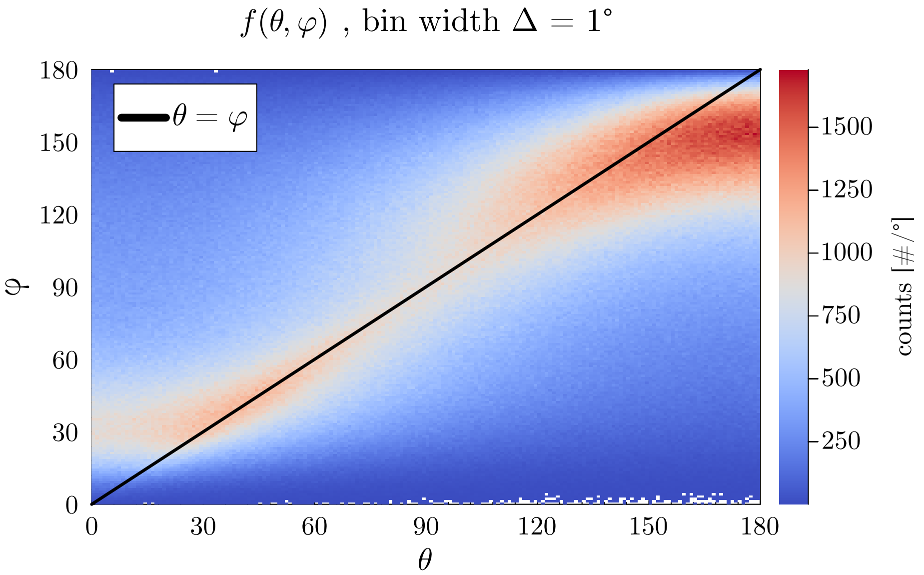

Figure 5.7: 2D Histgoram of the decay angle θ against the escape angle φ for a simulated uniform spectrum in θ. The solid black line depicts the perfect correlation $\theta = \varphi$. A bin width of $\Delta = 1°$ is used.

uniformly distributed spectra. This shows that the mentioned effects can be expected for any processes, regardless of the underlying DBD mechanism. Regardless, the φ distribution shape is still, to some extent, governed by the underlying θ distribution. It is thus important to understand, quantitatively, the transition from θ to φ in terms of the so-called detector response $f(\theta, \varphi)$. Here, depending on the input angular distribution, the measured φ distribution should differ. The next section is dedicated to a framework which quantifies the detector response to the decay angle.

5.2 Angular Correlation

The goal of this section is to quantify the angular correlations between the decay angle and the escape angle in a systematic manner via $f(\theta, \varphi)$. We aim to assess the impact of different data cuts on the angular correlation between θ and φ and develop a model to give meaning to the measured values of the escape angle and how to interpret them.

To achieve a more detailed understanding of the transition from θ to φ, as opposed to the relationship depicted in Figure 5.4a, we shift our focus to a two-dimensional (2D) distribution. Figure 5.7 illustrates a 2D histogram with θ along the x-axis and φ along the y-axis. We denote this distribution as $f(\theta, \varphi)$ to indicate that the relationship between θ and φ – the detector response function. Even though, ideally, a continuous function would be desirable, the limit of finite data points necessitates the use of a discrete representation - histograms. Typically, a bin width of either $\Delta = 1°$ or $\Delta = 5°$

is used [4]. Additionally, a black solid line representing $\theta = \varphi$ is displayed in figure 5.7. Events falling on this line indicate perfect correspondence, where the decay angle is identical to the escape angle. Any deviation, on the other hand, indicates a change in angle as the electrons traverse the foil. There are two regions with higher statistics visible in the figure – regions where red colored bins are dominant. These correspond to the two peaks seen in the φ distribution in the 1D distribution, figure 5.4a.

Besides quantifying $f(\theta, \varphi)$, in this section we make initial attempts at basic corrections which increase the correlation and reduce the uncertainty. This is done either via utilizing energy data-cuts (section 5.2.3) or by providing a way for *representing* the escape angle in terms of what the measurement most likely originated from - we denote this representation by φ' (section 5.2.4).

5.2.1 Horizontal Partitions of $f(\theta, \varphi)$

To perform a quantitative analysis of the angular correlations, we examine individual horizontal sections of $f(\theta, \varphi)$ presented in Figure 5.7. This is achieved by partitioning the data into intervals, where each section contains all θ values within a given range $\Delta\varphi \in (\varphi_{min}, \varphi_{max})$. This approach enables us to gain a detailed understanding of the underlying structure of $f(\theta, \varphi)$ and make conclusions about how the θ distribution affects the measured φ. Here, it should be emphasised that θ is not observable experimentally. We can only access θ from the simulation and must make informed decisions on it based on the measured φ.

By studying each section separately, we can calculate several statistical estimators of the θ distribution associated with that specific partition of φ. The statistical estimators computed include the mean, median, and mode of the distribution. These calculations let us establish a probability density function (PDF) that characterizes the likelihood of obtaining a particular escape angle value within a given $\Delta\varphi_i$ measurement, as a function of θ. Figure 5.8 shows a few of such partitions, along with their corresponding statistical estimators, marked by arrows on the x-axis. Several observations can be made:

1. The number of events within each partition (of equal width) varies depending on the origin of the partition. Partitions with very closed and very open φ contain fewer events compared to those with more moderate φ angles. This aligns with the conclusion drawn in section 5.1.

2. **The distribution of θ for each partition is very wide. The uncertainty on φ is large.** In other words, a single measurement of φ_i can arise from any θ value. This effect is particularly pronounced for angles close to $\sim 90°$, as evidenced

---

[4] The bin width is generally indicated in the caption of provided figures

by the shaded area representing the central 68% interval, which is widest in the case of perpendicular angles.

3. Conversely, the statistical estimators (mean, mode, median) align more closely with the position of the partition (detailed in the subfigure's title) for perpendicular φ values compared to more open or closed angles. The perpendicular case exhibits a greater uncertainty, however.

4. From the three statistical estimators, mode is generally closest to the *ideal correlation* $\varphi = \theta$, on the other hand, mean is generally the furthest.

The last point of the observations is shown in more detail in the Figure 5.9. Here, the y-axis represents the individual partitions $\Delta\phi_i$, with the corresponding statistical estimators plotted on the x-axis. The shaded area represents the central 68% band, plotted horizontally. Furthermore, the line $\varphi = \theta$ is shown in the figure.

5.2.2 k-lines

Up until now, our observations have been primarily qualitative. To enable quantitative comparisons of angular distributions and make informed decisions regarding potential data-cuts, we introduce the concept of angular correlation between θ and φ using what we call the k-lines. We then calculate the standard deviation (s) of the k distribution. We define k and s as:

$$k = \varphi - \theta, \tag{5.3}$$

$$s = \sqrt{\frac{1}{n}\sum_i k_i^2}. \tag{5.4}$$

For $k > 0$, it follows that $\varphi > \theta$, indicating that the measured angle overestimates the decay angle. Conversely, for $k < 0$, $\varphi < \theta$, which implies an underestimate. We construct k-lines as diagonal lines over $f(\theta, \varphi)$. Figure 5.10a shows an example of two k-lines. The red line in the figure represents cases where the escape angle is overestimated by 20°, while the blue line represents a 20° underestimation. By extending this approach, we can construct all possible k-lines covering the entire range of available angles and construct their histogram, as depicted in Figure 5.10b. The resulting figure has a peak around $k = 0$, representing perfect correspondence between φ and θ.

The width of the distribution can be characterized by s, which serves as a measure of error in the angular correlation. In the specific case depicted, s is found to be 46.99°, indicating an average deviation of φ from θ by approximately 46.99°. There is a rather large uncertainty on φ. The subsequent sections aim to explore strategies for reducing this error.

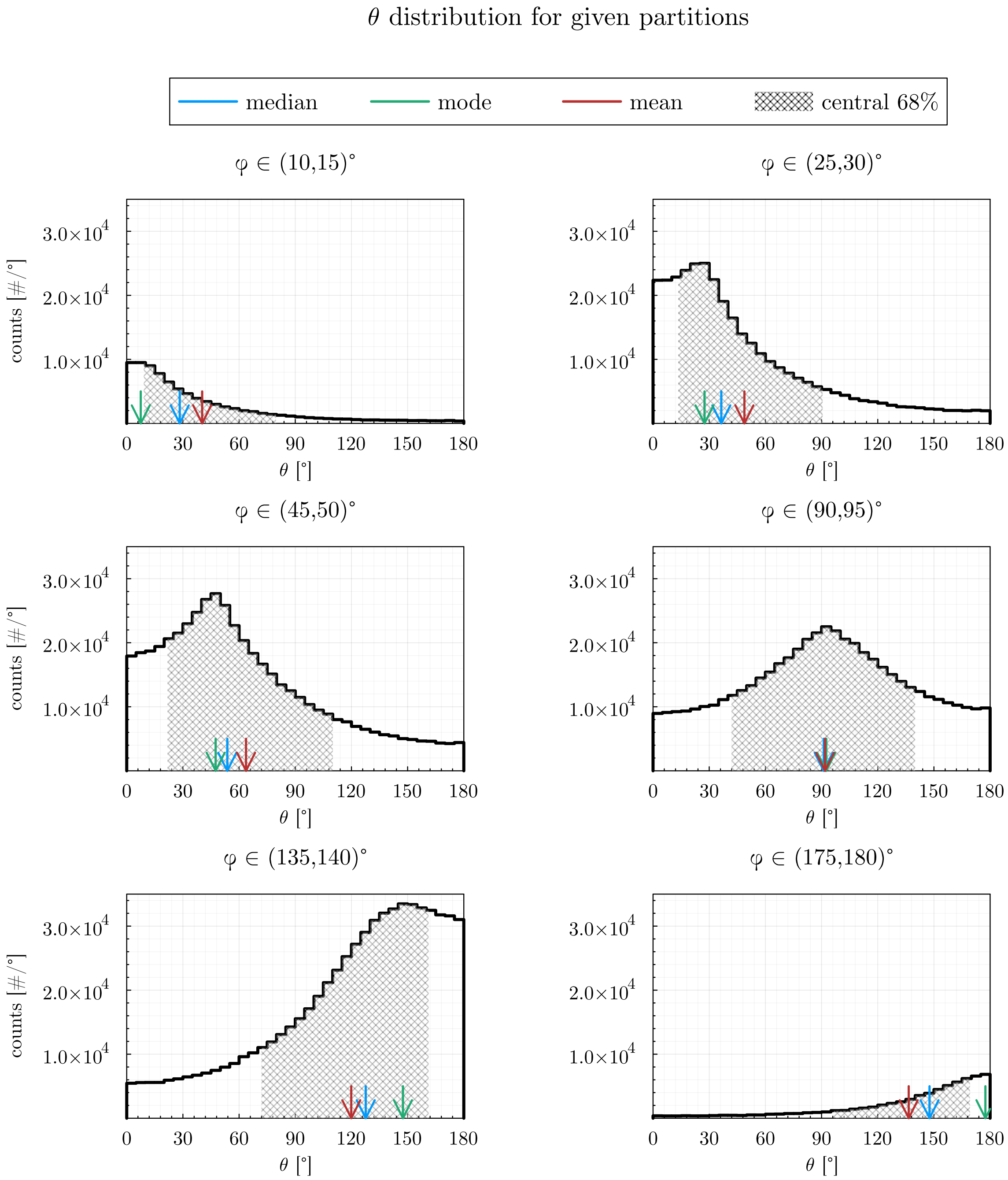

Figure 5.8: Horizontal partitions of the 2D distribution of θ vs φ. Each partition represents a section of the θ distribution, where the events belong inside partition of $\varphi \in (\varphi_{min}, \varphi_{max})$ are marked in the titles of the subfigures. The mean, mode and median of the distributions are indicated by vertical arrows, colored accordingly to the legend. A bin width of $\Delta = 5°$ was used.

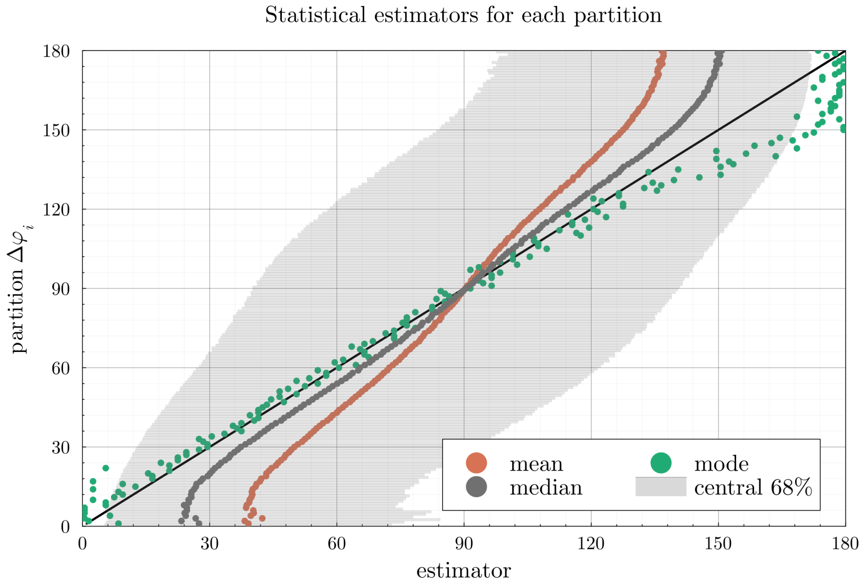

Figure 5.9: Statistical Estimators for Horizontal Partitions. Bin width of $\Delta = 1°$ was used.

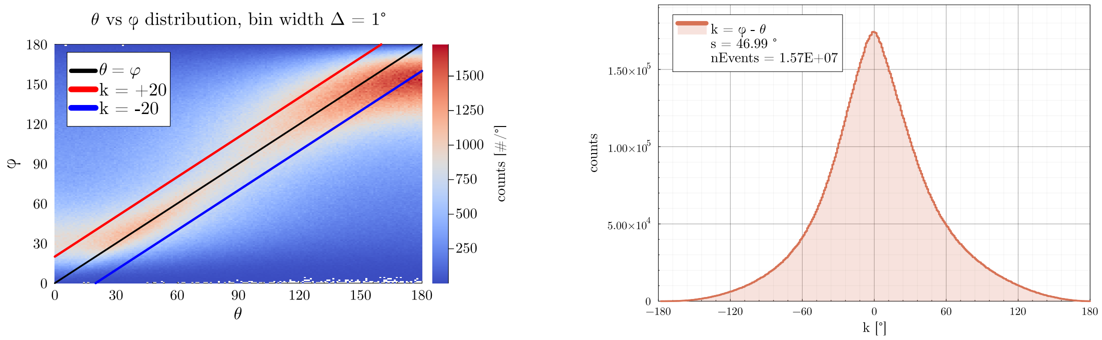

(a) 2D Angular Distribution θ vs φ with two k-lines depicted.

(b) Histogram of k-lines corresponding to all the possible k-lines obtained from 5.10a.

Figure 5.10: Definition of k-lines.

5.2.3 Energy Data-Cuts

One option to reduce the smearing of the decay angles, i.e. to obtain a better correlation between φ and θ, is to implement an energy data-cut on the data. As was shown in [30], correlation is better as energy increases. This is due to the fact that a higher energy electron is less prone to scattering as it travels through the volume of the source foil. Figure 5.11 shows $f(\theta, \varphi)$ for data where only events in which the sum of the electron energies (E_{sum}) lies within given limits $E_{sum} \in (E_{min}, E_{max})$.

The figure shows six sets of data, where the cut was applied with energy windows of $\Delta E = 500$keV. Two observations should be made. Both, the number of events and correlation increase with energy. The Figure 5.12 shows the six data-sets, however in the k-lines representation. Both unnormalized and normalized figures are shown to demonstrate the two observations – number of events and correlation (in terms of s). The best correlation is obtained, as expected, for the highest energies $E_{sum} \in (3000, 3500)$keV, with $s = 42.66°$. While, this is a better result than the previous one, the error is still entirely too large. Furthermore, the statistics has been reduced significantly.

5.2.4 Most Likely Origin

The main disadvantage of improving the correlation when using data-cuts is the reduced statistics. This problem can be avoided by using a different method that reduces s. The figure 5.8 shows the horizontal partitions with the statistical estimators. One may ask whether it is best to represent each partition in terms of some specific value, i.e. one of the estimators. In other words, we can ***interpret*** measured φ by some value φ'. For example, for the partition with $\varphi \in (25, 30)°$, the mode and the mean of the distribution are $\varphi_{i,mode} = 27.5°$ and $\varphi_{i,mean} = 48.8°$, respectively. This means, a measured value of an escape angle $\varphi_i = 26.2°$ which falls in range $\in (25, 30)°$ can be ***interpreted*** as $\varphi'_i = 27.5°$ if mode is used. On the other hand, the same measurement could be represented as $\varphi'_i = 48.8°$ if mean is used. Thus, in order to represent the measured value of an escape angle $\varphi = 26.2$, we have interpreted this measurement by *shifting* the data-point by some amount $\hat{s}$ so that the representation of the measurement φ' is believed to be *as close as possible* to the original decay angle θ. We can define φ' and $\hat{s}$ as follows:

$$\begin{aligned} \varphi' &= \varphi + \hat{s}, \\ \hat{s} &= \theta_{estimator} - \Delta\varphi_{bincenter}. \end{aligned} \tag{5.5}$$

Where $\hat{s}$ is the number representing an amount by which to *shift* the measured value of φ to obtain the representation φ'. $\theta_{estimator}$ is the value of the estimator (mean, mode, median, etc.) calculated from the θ distribution of the given partition. $\Delta\varphi_{bincenter}$ is the center value of the partition.

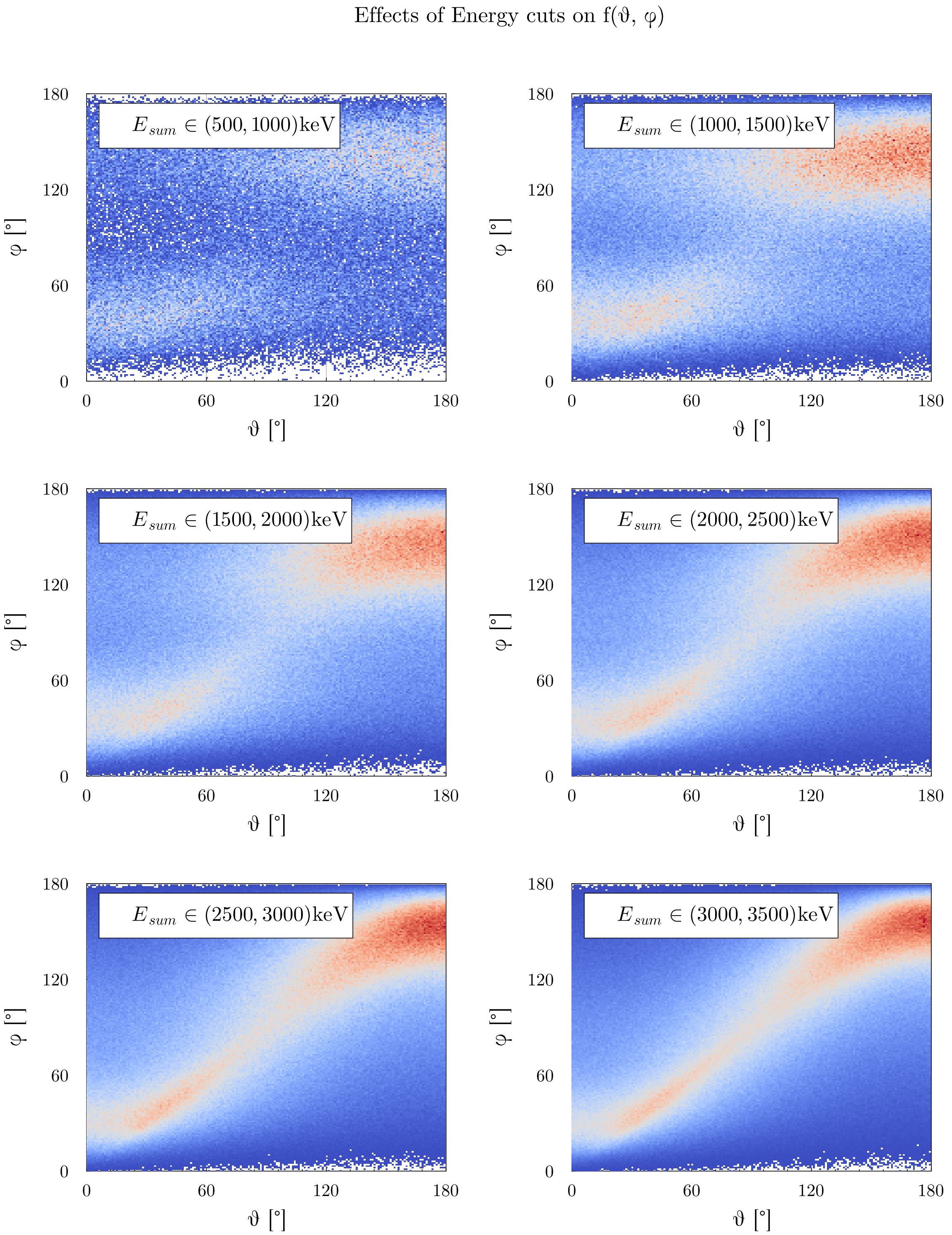

Figure 5.11: Effects of E_{sum} data-cuts on $f(\theta, \varphi)$. Bin width of $\Delta = 1°$, energy window of $\Delta E = 500$keV was used.

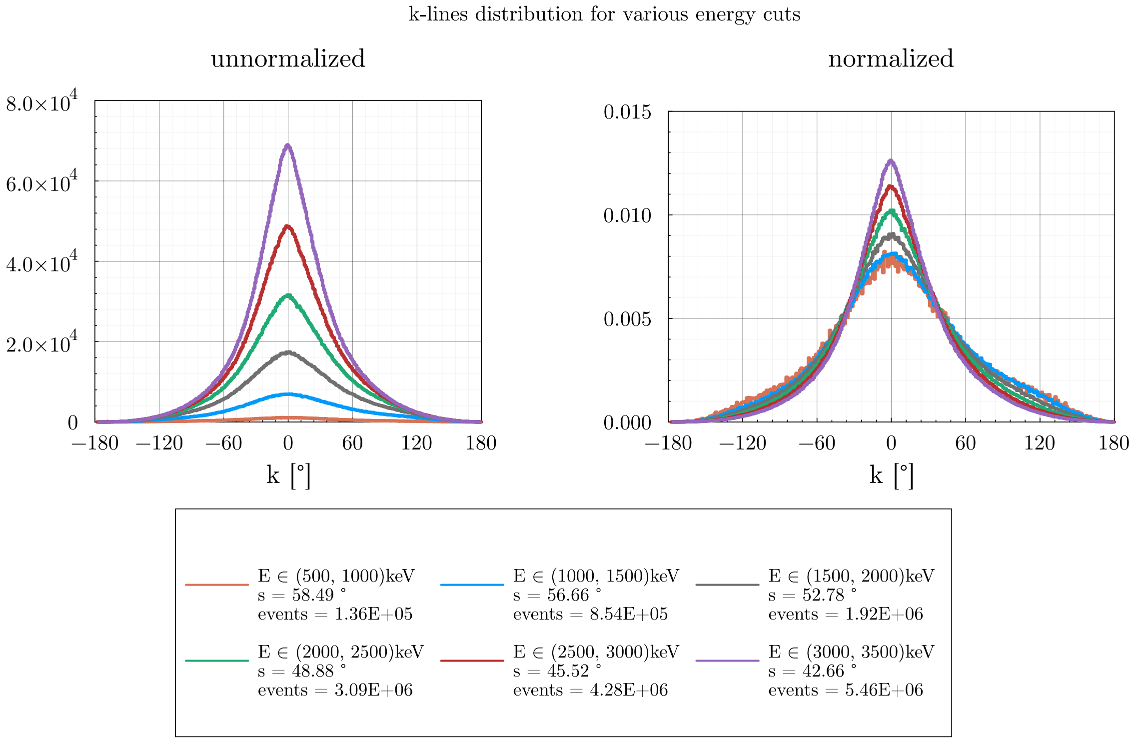

Figure 5.12: Effects of E_{sum} data-cuts on $f(\theta, \varphi)$ in k-lines representation. The unnormalized case is shown on the left, normalized is shown on the right. Bin width of $\Delta = 1°$, energy window of $\Delta E = 500$keV was used. The s and number of events for each case is displayed.

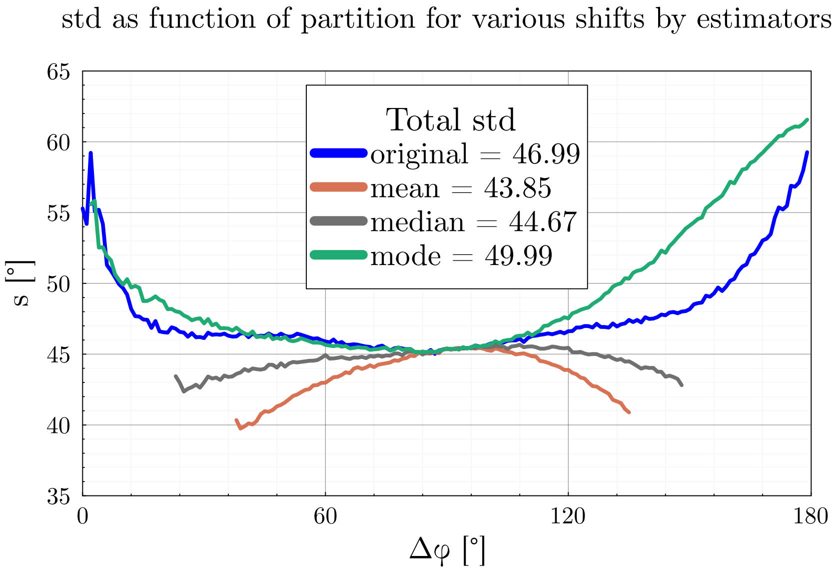
std as function of partition for various shifts by estimators

(a)

To figure out the effects of such shifting we follow the procedure:

1. we partition $f(\theta, \varphi)$ of the original data-set into small partitions, for example $\Delta = 1°$,
2. all k-lines are calculated for each partition along with their $\hat{s}$,
3. the corresponding estimators are calculated for each partition,
4. a shift is applied for each partition and using each estimator,
5. shifted k-lines and standard deviations are compared to the original distribution.

Figure 5.13a shows the standard deviations as calculated for each partition of the original $f(\theta, \varphi)$ and of distributions shifted accordingly to equation (5.5) for each estimator. The x-axis represents each partition, the calculated s is plotted on the y-axis. The legend also shows the total s of the distribution. It can be seen in the figure, that the best s is obtained when shifting by the mean value of the distribution. However, this also reduces the phase space most significantly. On the other hand, the representation by mode is even worse than the original, unmodified, distribution. Figure 5.13b shows the result of the applied methodology. On the x-axis is the measured escape angle φ with the y-axis showing the value by which to represent the measurement, φ'. It is obvious that such methodology for representing the whole partition by a singular number leads to too large an error and is an over-simplification.

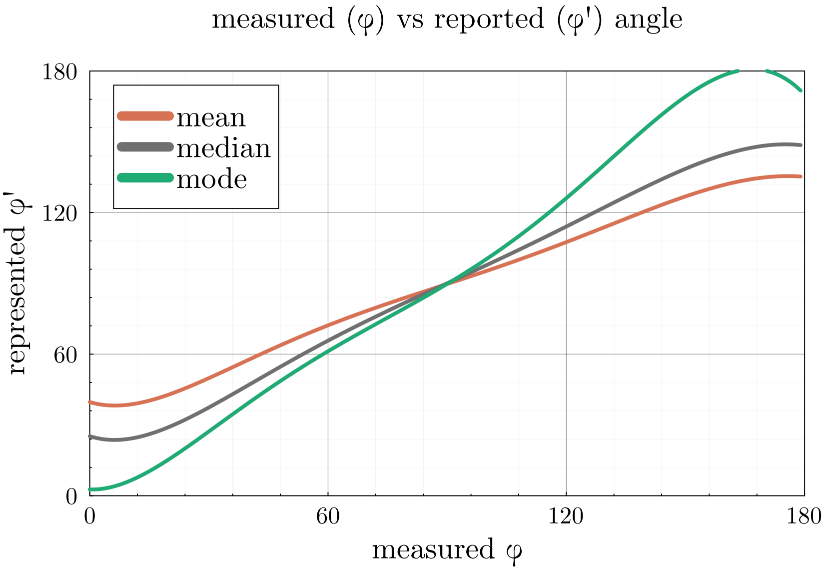

(b)

Figure 5.13: Comparison of shifts by each estimator. In 5.13a s is calculated for each partition $\Delta\varphi_i$ of the original $f(\theta, \varphi)$ distribution and distributions are shifted by the corresponding estimator. The total s of the distribution is shown in the figure legend. 5.13b shows representation of measured φ for different estimators.

5.3 Discussion

The potential of using the angular distribution for studying new physics drove the motivation of this section. If this observable is to be used for investigating the hidden DBD processes, it has to be thoroughly studied first. Section 5.1 qualitatively outlined the transition of θ to φ, replicating the methodology from [30] with a more generalized approach – by using uniform input spectra. The conclusion drawn is that the φ shape is notably influenced by detector geometry and reconstruction algorithms, rather than the underlying physics of the studied DBD process. This underscores the necessity of introducing a quantitative approach through estimating the detector's response function $f(\theta, \varphi)$. Each process is expected to have *slightly* different response function. The methodology for obtaining the response function is presented in the first part of section 5.2.

It was shown that by applying energy data-cuts the correlation can be increased. This opens up the question whether by implementating various other modifications to the data, or even the detector itself could also present a means for improving the detector response. The methodology is wrapped into a generalized software framework, and as such can easily be repeated on various simulated data-sets with different simulation settings. In the future work, the configuration with magnetic field turned off will be studied. This should remove the cases where, under the magnetic field, particles emitted along the source foil return into the foil, which should present a potential improvement. On the other hand, the discrimination between signal and background events would be decreased. It remains to be determined whether having the magnetic field turned off will be an improvement or not. Furthermore, once the new tracking algorithm is fully incorporated in the *Falaise*, the analysis will be repeated and results evaluated. An increase in precision is expected. Lastly, the analysis shall be repeated and the response function calculated for the various DBD modes presented in chapter 2. The study of these is the subject of this project.

The last part of this chapter dealt with evaluating the uncertainty of $f(\theta, \varphi)$ and exploring possible improvements to it. In fact, the product of presented analysis was an attempt to solve, in the most simple-way, the unfolding (or deconvolution) problem, which involves inferring the true value (θ) from measured data (φ) [60]. There are, in fact, more powerful methods of unfolding, via the so-called regularized unfolding (which corrects for uncertainties to some extent), which can potentially lead to better results than the one we obtained here. However, the unfolding works best when the intrinsic uncertainty is small. This, unfortunately, is not the case for the measurements of escape angle. As stated in [60] it is often more appropriate, rather than trying to unfold the measured data, to simply *fold* the theoretical predictions. In practical terms, this means applying the smearing effect (represented by the response function $f(\theta, \varphi)$) to theoretical predictions. Implementing this will be one of the main aims of the future work on this project, the justification for it is presented in the following chapter 6.

CHAPTER 6

SUPERNEMO FEASIBILITY STUDY

One of the objectives of the SuperNEMO experiment is to study exotic physics potentially hidden in $2\nu\beta\beta$. The detector's unique design allows measurements of full topology of the event, particle identification and it measures several kinematics variables of the decay. This makes the subtle differences in predicted spectra between different processes (as described in section 2.1) observable. Ultimately, once data is measured, a data-set containing events with three variables is obtained. These are the two electron energies and the angle between them. The data can be compared to the predictions from theory using various methods of fitting the spectra. Subsequently, one determines the value of the parameter which envelops the studied $2\nu\beta\beta$ process – i.e. in the case of refined $2\nu\beta\beta$ spectra (section 2.5) the parameters ξ_{31} and ξ_{51}.

However, the first step, before attempting to fit the spectra, is to answer the question whether SuperNEMO is capable of measuring enough statistics to confidently overcome uncertainties due to statistical fluctuations. Can SuperNEMO confidently measure the subtle differences presented in the spectra?

The following chapter describes, using a so-called *toy model example*, the methodology we have implemented in order to determine the feasibility to study various processes with SuperNEMO. A dedicated framework was developed with the objective of estimating the minimal number of events SuperNEMO must measure to differentiate between two slightly distinct spectra, surpassing statistical uncertainties in comparison.

The reason for this is to determine, whether subsequent fitting of the spectra is worthwhile. The *toy model* presented in section 6.1 compares two simulated data-sets, the *"standard"* $2\nu\beta\beta$ spectra as used commonly today are compared to the more precise calculation of $2\nu\beta\beta$ spectra described in section 2.5 which we named the *"refined"* spectra. In particular, we compare the single electron energy distribution and the angular distributions of each. The latter takes advantage of the findings presented in chapter 5.

This methodology will be subsequently repeated for each process of interest, before efforts to fit the spectra are made.

6.1 Toy Model: Minimum Events Required

6.1.1 Description of Simulation Setup and Input Data

As mentioned above, the methodology presented here compares two simulated spectra. The *standard* and the *refined* spectra were chosen for this purpose.

The calculation of the standard $2\nu\beta\beta$ decay rates is explained in section 2.4, and it is implemented in the Falaise simulation software. The single electron energy distribution for this process is based on equation (2.15), and the angular distribution is given by:

$$\frac{d\Gamma^{2\nu}_{st.}}{d(\cos\theta)} \propto 1 + K^{2\nu}_{st.}\cos\theta, \tag{6.1}$$

where $K^{2\nu}_{st.} = -0.88$ is the angular correlation factor for the standard spectrum.

To simulate the refined spectra (and other custom processes), a dedicated library called MPGenbb [61] was developed. An input for this library is a set of differential phase space factors $\frac{dG_i}{dE_1 dE_2}$ calculated by Šimkovic et al. [5], which are converted into suitable input for Falaise as described in section 3.2. The single electron energy decay rate is given by:

$$\frac{d\Gamma}{dT_e} \sim \frac{dG_0}{dT_e} + \xi_{31}\frac{dG_2}{dT_e} + \frac{1}{3}(\xi_{31})^2\frac{dG_{22}}{dT_e} + (\frac{1}{3}\left(\xi_{31}\right)^2 + \xi_{51}\big)\frac{dG_4}{dT_e}, \tag{6.2}$$

where T_e is the kinetic energy of an electron, and G_i are the phase space factors from the Taylor expansion as described in section 2.5. For this *toy model* analysis, the values $\xi_{31} = 0.60$ and $\xi_{51} = 0.14$ were used in generating the simulated data-set. These values correspond to one of the sample cases calculated in [5].

The angular distribution for the refined spectrum is given by:

$$\frac{d\Gamma^{2\nu}_{ref.}}{d(\cos\theta)} \propto 1 + K^{2\nu}_{ref.}\left(\xi^{2\nu}_{31}, \xi^{2\nu}_{51}\right)\cos\theta. \tag{6.3}$$

The angular correlation factor $K^{2\nu}_{ref.}(\xi^{2\nu}_{31}, \xi^{2\nu}_{51})$ is described by the equation:

$$K^{2\nu}_{ref.}(\xi^{2\nu}_{31}, \xi^{2\nu}_{51}) = -\frac{H^{2\nu}_0 + \xi^{2\nu}_{31}H^{2\nu}_2 + \frac{5}{9}(\xi^{2\nu}_{31})^2 H^{2\nu}_{22} + (\frac{2}{9}(\xi^{2\nu}_{31})^2 + \xi^{2\nu}_{51})H^{2\nu}_4}{G^{2\nu}_0 + \xi^{2\nu}_{31}G^{2\nu}_2 + \frac{1}{3}(\xi^{2\nu}_{31})^2 G^{2\nu}_{22} + \left(\frac{1}{3}(\xi^{2\nu}_{31})^2 + \xi^{2\nu}_{51}\right)G^{2\nu}_4}. \tag{6.4}$$

Here, $G^{2\nu}_i$ and $H^{2\nu}_i$ $(i = 0, 2, 4, 22)$ are kinematical factors originating from the integration over the phase-space. For $\xi_{31} = 0.60$ and $\xi_{51} = 0.14$, the corresponding angular correlation factor is $K^{2\nu}_{ref.} = -0.66$. The relationship between ξ_{31} and $K^{2\nu}_{ref.}$ for a fixed ξ_{51} is shown in Figure 6.1a. It should be noted that the value of ξ_{31} is bounded within

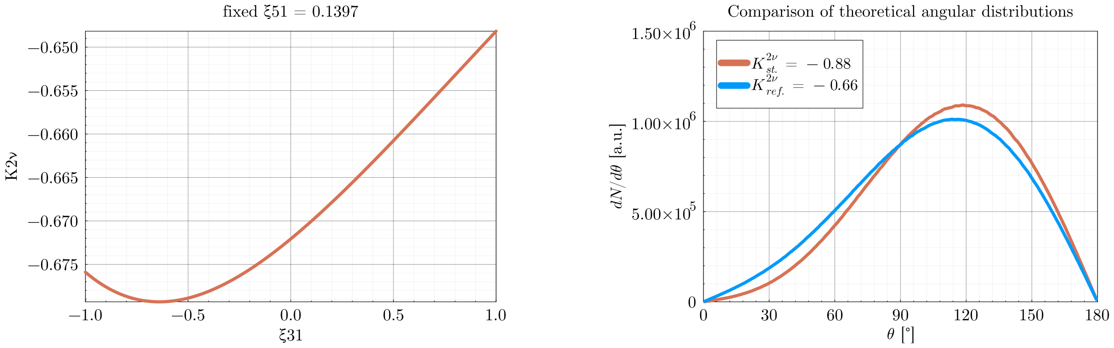

(a) $K^{2\nu}_{ref.}(\xi_{31}, \xi_{51} = 0.14)$.

(b) Theoretical angular distributions.

Figure 6.1: Left: $K^{2\nu}_{ref.}(\xi_{31}, \xi_{51} = 0.14)$. Right: comparison of theoretical angular distributions for $K^{2\nu}_{st.} = -0.88$ and $K^{2\nu}_{st.} = -0.66$.

range $(-1, 1)$ [5]. The corresponding $K^{2\nu}_{ref.}$ changes only very slightly. Thus, the angular distribution measurements must be exceedingly precise to distinguish the changes. This is supported in Figure 6.1b, which compares theoretical angular distributions for the two values of $K^{2\nu}$.

For the comparison of processes and to determine SuperNEMO's sensitivity, both data-sets were simulated using a common setup. Each simulation involved 10^8 events, and the default magnetic field ($\approx 25G$) was used in Falaise to enable particle charge determination. The effect of turning off the magnetic field, as discussed in chapter 5 is one of the possible aspects for future analysis. The analysis will be repeated with the magnetic field turned off.

The events were filtered using data-cuts described in section 5.1, approximately 8% of events passed the cuts. The decreased efficiency in comparison to the uniform spectra presented in chapter 5 is attributed to the shape of the energy distribution of $2\nu\beta\beta$. As seen in figure 2.2, the spectrum has its peak in the lower energy regions. As shown in 5.2.3 lower energy electrons are less likely to pass the data-cuts.

The simulation output provided pairs of *reconstructed* electron energies and escape angles (φ) for each event. To obtain *reconstructed* energies, the *mock* calibration was used, described in 3. No background was considered at this stage.

Figure 6.2 displays the comparison between the *reconstructed* single-electron energies and angular distributions. Two notable qualitative features can be observed from the figure. First, the largest residuals occur at the edges of the distribution for both the angular and energy spectra. Second, the edges of the energy distribution (at very low and very high energies) exhibit the most extreme residuals, but the amount of statistics in these regions is limited, affecting the reliability of the information. Excluding these regions, the differences in the distributions are generally within less than 10% of each other. Furthermore, the angular distribution shown exhibits similar shape as the one

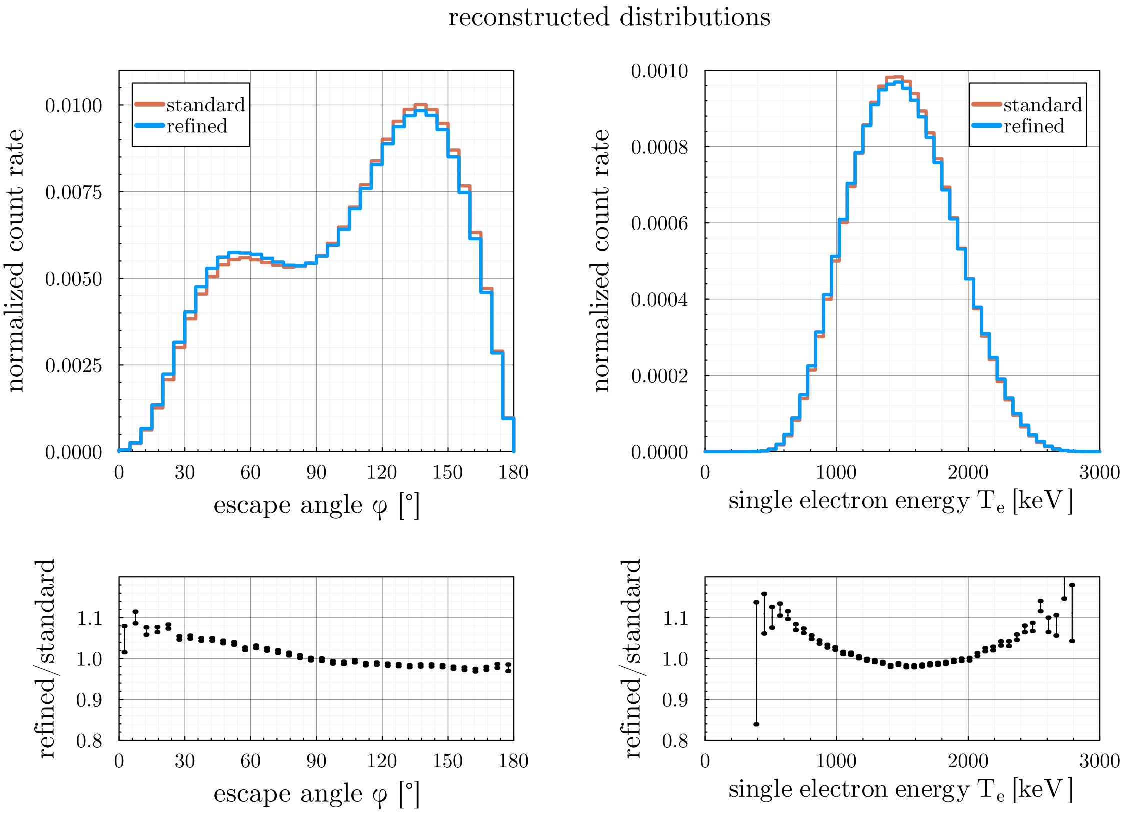

Figure 6.2: Simulated angular and single-electron energy distributions for standard (red line) and refined (blue line) $2\nu\beta\beta$. The events shown have passed through the data-cuts. The residuals between refined and standard spectrum is shown at the bottom.

depicted in figure 5.4a. This supports the conclusion that the detector geometry and design have the strongest influence on the shape of the measured angular distribution.

Once SuperNEMO accumulates sufficient $2\nu\beta\beta$ data, the spectra will be fitted to determine the values of presented parameters. In this section, the goal is to determine whether such an example of a refined spectrum can be distinguishable from the standard spectrum within SuperNEMO. The following section describes the methodology to do so.

6.1.2 Statistical Analysis

When attempting to compare two slightly different spectra, the amount of data measured must be enough as to confidently overcome the statistical fluctuations. An example of comparing two simulated data-sets of different sample sizes from the standard and refined spectra is shown in figure 6.3. The figure shows energy and angular distributions of data-sets with $20,000$ events and $1,000,000$ events. The residuals are also shown for each. It can be seen, from the residuals plot, that for the smaller sample size, the statistical uncertainty is rather large, as would be expected. The aim of the presented analysis is to say which sample size confidently overcomes this uncertainty. This sample size is then marked as the minimum required statistics to be measured.

To estimate the number of events needed for SuperNEMO to reliably distinguish the subtle differences in the spectra and enable subsequent parameter fitting, a statistical analysis using two methods of hypothesis testing was applied. These tests are commonly used to assess whether two data-sets originate from same (or different) underlying distributions. The null hypothesis (H_0) for the tests assumes that the data-sets follow the same underlying distribution. One data-set is considered as the reference (*standard* spectrum) against which the other data-set (*refined* spectrum) is compared. The alternative hypothesis is that the two data-sets are **not** from the same distribution. The goal is to reject H_0, indicating a significant difference between the two data-sets.

The two methods applied to the simulated data are: Pearson's chi-squared test (χ^2) [62, 63] and the Kolmogorov-Smirnov test (KS) [64, 65]. Each test's outcome yields a test statistic and a corresponding $p-value$, which helps assess the likelihood to reject the null hypothesis.

Description of the Hypothesis Tests

χ^2 Hypothetsis Test

In the χ^2 test, the two data-sets are compared by constructing test statistics from their histograms, each divided into N bins. The test statistic is given by:

$$\chi^2 = \sum_{i=1}^{N} \frac{(O_i - E_i)^2}{E_i}, \tag{6.5}$$

where O_i is the observed number of events in bin i of the compared data-set, and E_i is the expected number of events in bin i of the reference data-set, which serves as the *expectation.* The χ^2 test assumes that O_i follows a Poisson distribution with mean value E_i, and that each bin satisfies the condition $O_i, E_i > 5$. Under these assumptions, the observed test statistic should follow a χ^2 distribution with $N-1$ degrees of freedom. The $p-value$ is then calculated, and its value is compared to a *critical value* α, representing the significance level. For example, if $\alpha = 0.05$ and the obtained $p-value$ is less than α, H_0 is rejected.

However, the χ^2 goodness of fit test has some disadvantages. It is sensitive to the binning used in construction of the histogram. Moreover, to satisfy the condition that $O_i, E_i > 5$, adjustments may be required for the range on the x-axis and the bin-width. These adjustments are specified in the text whenever the χ^2 results are presented. In the case of this *toy example* the binning is as follows:

1. for the angular distribution the full range of $(0, 180)^\circ$ was divided into bins with width of $\Delta\varphi = 15^\circ$,

2. for the energy distribution the range of $(450, 2100)$ keV was divided into bins with width of $\Delta E = 150$ keV.

KS Hypothesis test

For the KS test, Empirical Cumulative Distribution Functions (ECDF[1]) are constructed for both data-sets. The test statistic for the KS test is the largest absolute difference between the two ECDFs, denoted as D. An illustration of this is shown in figure 6.4b. The p-value is then calculated from the so-called Kolmogorov distribution. Example of the distribution is shown in figure 6.4a. The drawback of the KS test is that it is less sensitive at the tails of the distributions, where the largest differences are expected in the case of our spectra of interest (*standard* and *refined*).

Summary

Each test is more suitable in different situations, depending on factors like the shape of the underlying distribution and the number of events. This can lead to inconsistencies in the results. Hence, it is crucial to perform each test on the data and choose the appropriate one. We decided to draw conclusions from the method that gives the most conservative results.

A common approach for enhancing the robustness of hypothesis tests involves iteratively applying the test on various subsets from the compared data sets. For instance, the test is repeated N times by extracting N random subsets from the distributions, each with a defined sample size (n). The subsets are then subjected to the hypothesis test, producing a test statistic and its associated p-value is calculated (generally done via a software library). For example, we can take 500 subsets from the two simulated angular distribution data-sets, $N = 500$, with sample size $n = 20,000$ events in each (the spectra are shown in figure 6.3a). Then we compare the N-pairs of spectra via the χ^2 test and the KS test and calculate the corresponding test statistics. The figure 6.5 shows the results of such methodology. Here, for the χ^2 method, the previously described binning for the angular distribution was used. Thus, with bin width of $\Delta\varphi = 15°$, the corresponding degrees of freedom ($d.o.f.$) for the χ^2 test is 11. For a significance level of $\alpha = 0.1$ and $d.o.f. = 11$, a χ^2 value greater than 17.275 is required to reject the hypothesis. The histogram indicates that only a subset of tests satisfied this condition. The KS test yielded a test statistic distribution following the Kolmogorov distribution. However, an approximation method is necessary to compute the p-values in such a case. Regardless, the two figures show that the results of the tests are influenced not only by the sample size and the underlying distributions, but

---

[1] ECDF is a distribution function which is constructed by first ordering the data-set and then summing each empirical observation in a set of n observations by a value of $1/n$.

also by the statistical fluctuations stemming from randomly drawing data. This, of course, is an expected outcome.

In this project, all of the tests were conducted using the HypothesisTests.jl [66] library from Julia programming language [67].

6.1.3 Evaluation Procedure

To perform the analysis, including the results from last section, we have chosen the following approach. In performing the hypothesis tests, the two data-sets which we compared were split randomly into batches of varying sample sizes, each containing 100 subsets, $N = 100$. The sample sizes vary in range of $n \in (2 \times 10^4 - 10^6)$ events in each subset.

We calculate the $p - value$ for each hypothesis test for each subset of a specific sample size, and thus gain 100 $p - values$ for each combination. Figure 6.6 shows the distribution of $p - values$ for a KS test comparing the single-electron energy distributions for the subsets of sample sizes specified in the x-axis. It can be seen in the figure that the calculated $p - value$s vary widely for smaller sample sizes. As expected, when hypothesis test does not reject H_0, the $p - value$s are uniformly distribution. Increasing the sample size increases the probability to reject H_0.

The procedure is repeated in three more combinations: KS test for the angular distribution, and χ^2 tests for angular and energy distributions. The results are shown in figure 6.7. It can be seen that, here, the p-values approach 0 much more quickly than in the case of KS test for the single-electron energy distribution. However, the results still fluctuate for smaller sample sizes.

To show the results from a different perspective, we calculate the mean $p - value$ for each combination. The means of the calculated $p - value$s for all combinations are shown in figure 6.8. It can be seen that the KS test is the more conservative of the two. However, as shown in figure 6.6 the calculated $p - value$s fluctuate a lot.

In order to better evaluate the effectiveness of the individual tests, we calculate the efficiency to *reject* H_0. The efficiency is defined as:

$$\varepsilon_{reject,H_0} = \frac{n_{rejected,H_0}}{n_{total=100}}. \tag{6.6}$$

In order to convincingly extract which sample size already contains large enough statistics to distinguish the two compared spectra, a condition is proposed: *the best sample size to use is chosen as the sample size where three consecutive values of* ε_{reject,H_0} *are* 100%. Figure 6.9 shows the calculated efficiencies for the combination of four tests and distributions for $CL = 90\%$. The uncertainties on the efficiencies were calculated based on the method described in [68].

CL	**KS: angle**	**KS: energy**	χ^2**: angle**	χ^2**: energy**
0.683	90,000	250,000	60,000	70,000
0.900	200,000	350,000	80,000	100,000
0.954	200,000	350,000	80,000	200,000
0.997	250,000	550,000	200,000	250,000

Table 6.1: Results of the combinations of goodness of fit tests for various CL.

The smallest sample sizes, which fulfilled the given condition for three CLs, are marked in the table 6.1. It can be seen that KS test is more stringent than χ^2. Furthermore, in order to distinguish two angular distributions less measured events are required than in the case of the single-electron energy spectra. However, Due to the fact that for each $2\nu\beta\beta$ event, there are two entries for energy, but only one for the angle, the single-electron energy distribution has effectively twice as much statistics. These results also rely on the quality of the input data. For example, in angular distribution, the new tracking algorithm, once implemented, will affect the angular resolution of the measured φ.

Using, for example $CL = 90\%$, the required minimum statistics for distinguishing the two spectra ranges from $80,000$ for a χ^2 test in angular distribution up to $350,000$ for a KS test on energy distribution. We calculate, as a very crude estimate, the number of events observed n_{OS} for SuperNEMO from equation (2.15) to be around $> 250,000$ for an expected exposure of $17.5kgy$ [69] and assumed efficiency $\varepsilon = 0.3$. In conclusion, the required amount of statistics should be achievable within the scope of data-taking campaign of SuperNEMO.

6.2 Discussion

The methodology introduced in this chapter is a versatile framework which can be applied for comparison of various combinations of the $2\nu\beta\beta$ spectral hypotheses. The software created during this process serves as a general tool, reliant merely on input from the theory. The results demonstrate that, at a minimum, distinctions between the standard and refined spectra should be observable within SuperNEMO's data-taking campaign. The effects of magnetic field and new track reconstruction algorithm are to be determined in the near future. Nevertheless, even with the most conservative estimate, using the KS method to distinguish the *toy model*'s spectra it is enough to measure 200,000 events at a $CL = 90\%$ to distinguish the angular distributions. It should be noted, that this is a order of magnitude estimate, as the results of the hypotheses tests applied in the presented methodology fluctuate statistically.

In order to perform the real data analysis in near future, two approaches are under consideration. The first approach takes advantage of methods which unfold the detector response functions. In such case, the measured data is effectively translated into the theoretical context. Here, the theoretical prediction is compared with the assumed theory that generated the measured data. An alternative approach is the folding of theoretical predictions. In essence, once the detector response functions are understood, they are applied to theoretical predictions, enabling a direct comparison with measured data.

In either case we start with the following methodology. We treat the DBD events as a random variables x which follow the PDF describing the given studied DBD process. The PDF will be a function of three varibales: *true* electron energies E_1 and E_2 and the decay angle θ, and the *true* parameter(s) encompassing the process ξ. We can denote this PDF as $\rho(E_1, E_2, \theta; \xi)$.

In case of the unfolding approach, if the detector response functions for the energy and angular dependence can be reliably unfolded, then $\rho(E_1, E_2, \theta; \xi)$ can be extracted from data and fit to the theoretically predicted PDF to extract the parameter of interest. This means, we are attempting to reconstruct the theory from measured data.

The approach of folding, which is more commonly implemented in research, the opposite direction is taken. We move from theory to measured data by smearing the theoretical predictions with known detector responses. The smeared theoretical spectrum is then described by:

$$\int \rho(E_1, E_2, \theta; \xi) f(E_1' - E_1) f(E_2' - E_2) f(\theta - \varphi) dE_1 dE_2 d\theta. \tag{6.7}$$

Here, the $f(E_i' - E_i), i \in (1, 2)$ are the PDFs describing the detector energy resolution for a measured electron energies E_1 and E_2, i.e. Gaussian distribution:

$$f(E_i' - E_i) = \frac{1}{\sigma\sqrt{2\pi}} e^{-\frac{1}{2}(\frac{E_i - E_i'}{\sigma})^2}, \tag{6.8}$$

the $f(\theta - \varphi)$ is the angular detector-response function. As depicted in the chapter 5 the response function is a matrix, so the evaluation of the integral will not be trivial.

For the purpose of estimating the parameter of interest, the method of Maximum Likelihood Estimate (MLE) can be used [60]. The method gives a framework to estimate the parameters which best describe a set of measured data.

Each DBD event can be treated as an independent measurement x_i governed by the PDF $\rho(x_i; \xi)$ as described above. The likelihood function L is described as the joint PDF for all measurements i, and is a function of the parameter ξ:

$$L(\xi) = \prod_i \rho(x_i; \xi). \tag{6.9}$$

We can calculate the most probable estimators for ξ parameters as the ones which maximize the likelihood function:

$$\frac{\partial L}{\partial \xi} = 0. \tag{6.10}$$

Thus, the solution to the equation 6.10 gives the value of the desired parameter(s) of interest.

The main aim of the future activities in this project is to test the two approaches and extend the presented framework to establish the most efficient analysis procedure. The first SuperNEMO physics data is expected for first half of year 2024 (after the finalization of the passive shielding). Our analysis procedure will be applied on the SuperNEMO data from these early phases.

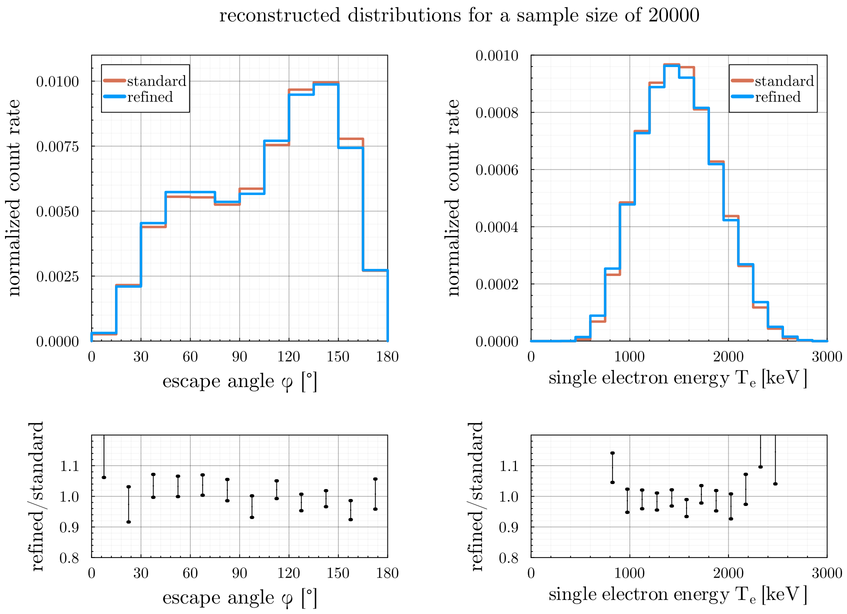

(a) $20,000$ events.

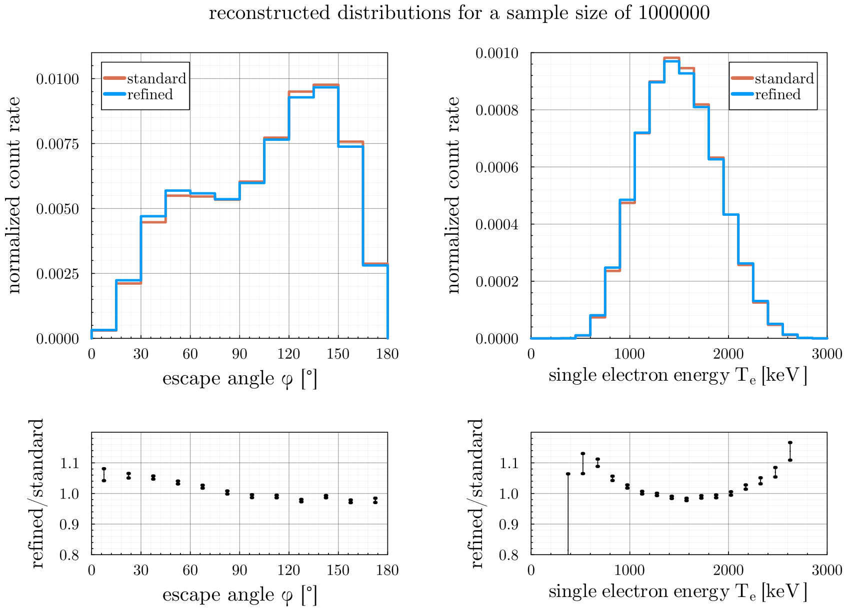

(b) $1,000,000$ events.

Figure 6.3: Reconstructed spectra for a sample size of $20,000$ (6.3a) and $1,000,000$ (6.3b) simulated events. Histograms were constructed with the following bin widths: $\Delta\varphi = 15°$ and $\Delta E = 150$keV, for the angular and energy distributions, respectively.

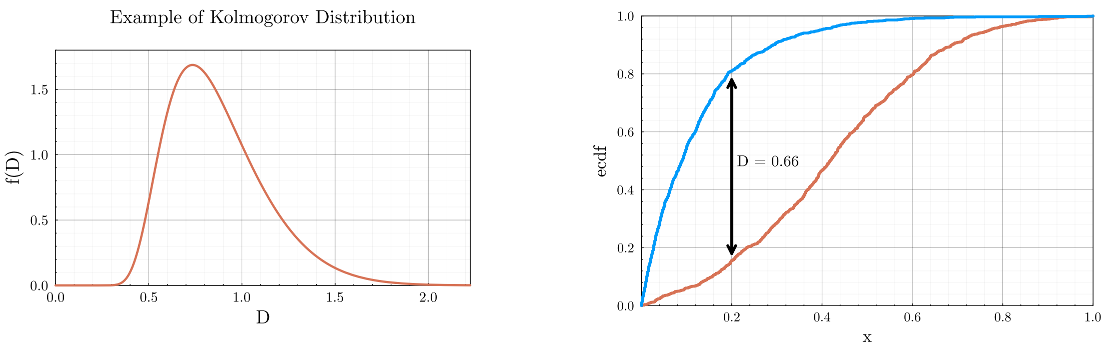

(a) Kolmogorov distribution.

(b) ECDF.

Figure 6.4: Left: Example of Kolmogorov distribution. Right: Example of two ECDFs for two sample data-sets. The maximum difference is marked as D.

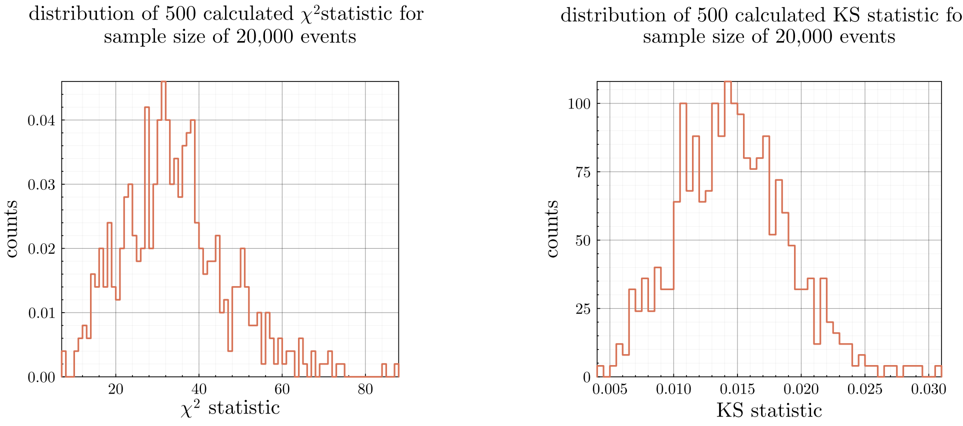

(a) χ^2 test.

(b) KS test.

Figure 6.5: Distributions of calculated test statistics for $N = 500$ tests of sample size $n = 20,000$ of the compared angular distributions. On the left are the calculated χ^2 statistics and on the right the calculated KS statistics.

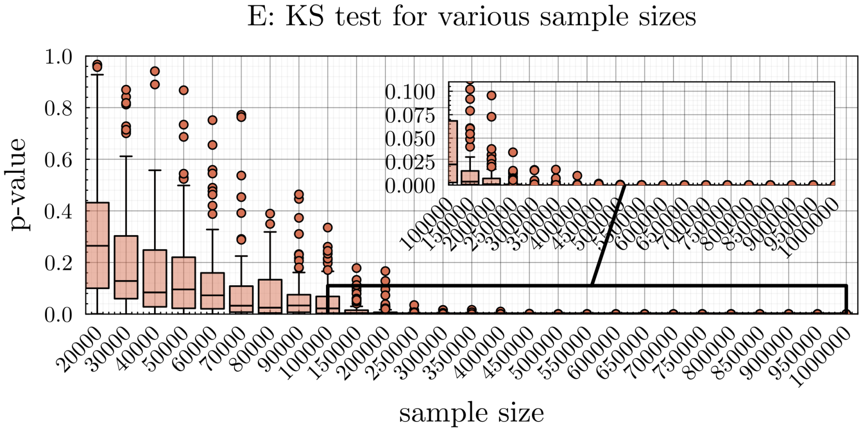

Figure 6.6: $p - values$ of a KS test for single electron energy distribution for various sample sizes, specified on the x-axis. The median of the distribution is shown as the horizontal black line within the box. The upper and lower bound of the colored box represent the first quartile Q1 (25%) and the third Q3 (75%), respectively. The whiskers represent 1.5 multiple of the interquartile range between Q1 and Q3. The outliers are shown as dots.

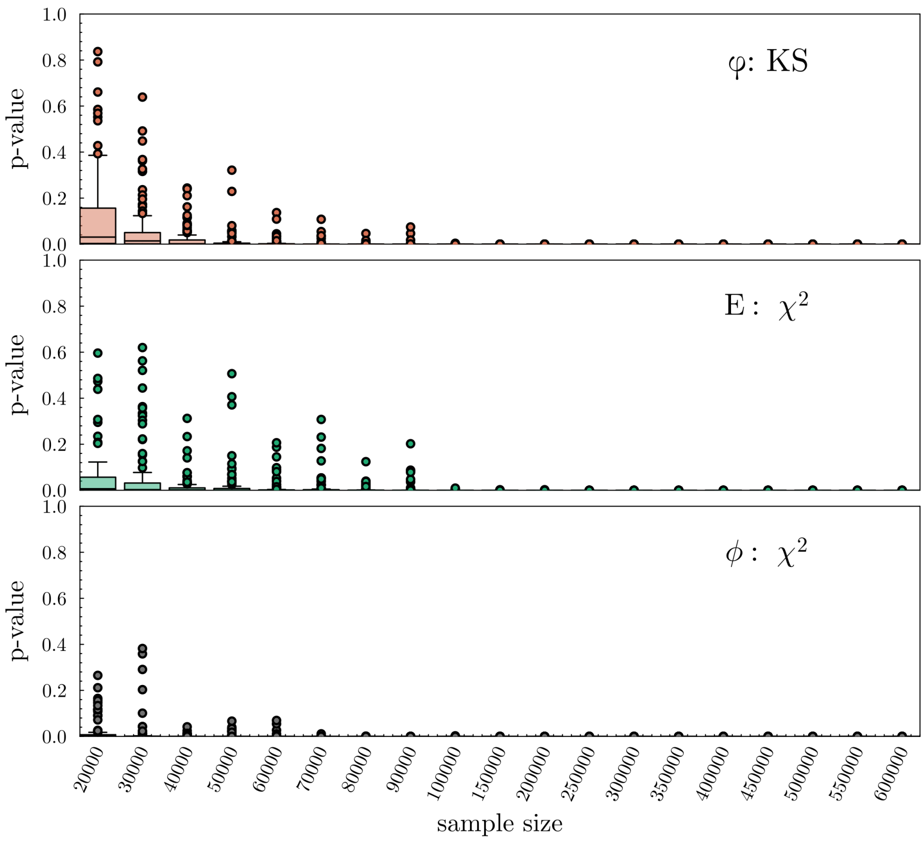

Figure 6.7: $p - values$ of a KS: angle, χ^2: energy, χ^2: angle.

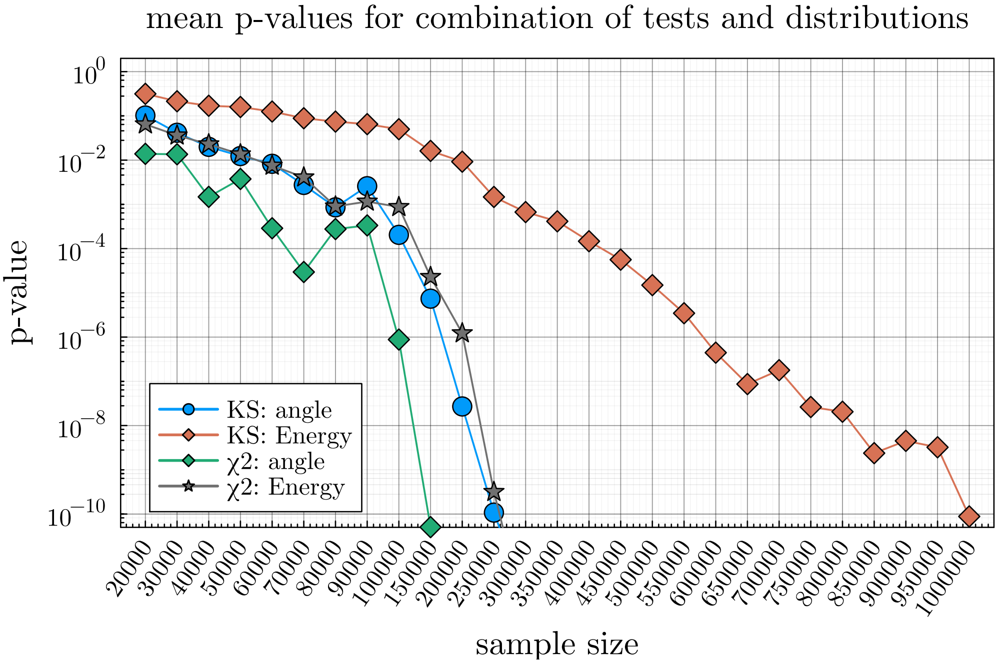

Figure 6.8: Mean $p-values$ for KS and χ^2 tests.

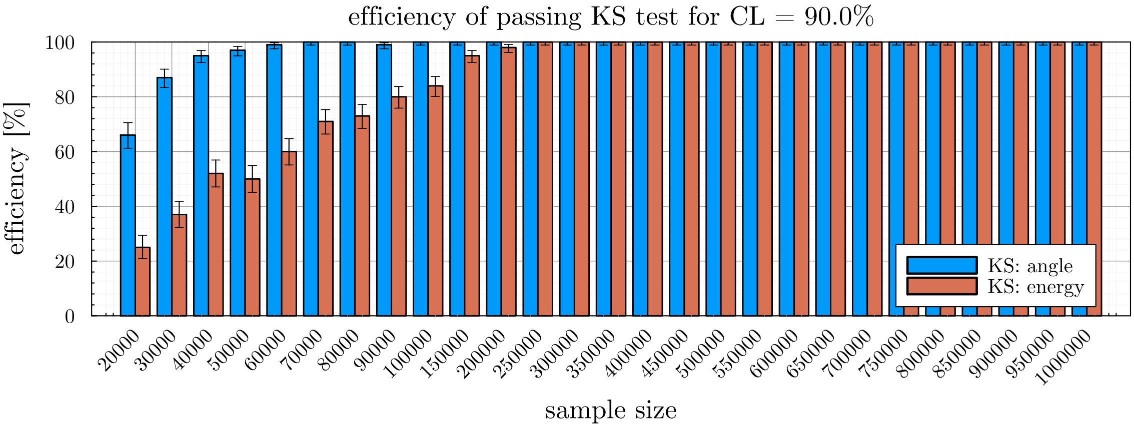

(a) ε_{reject,H_0} for KS test at $CL = 90\%$.

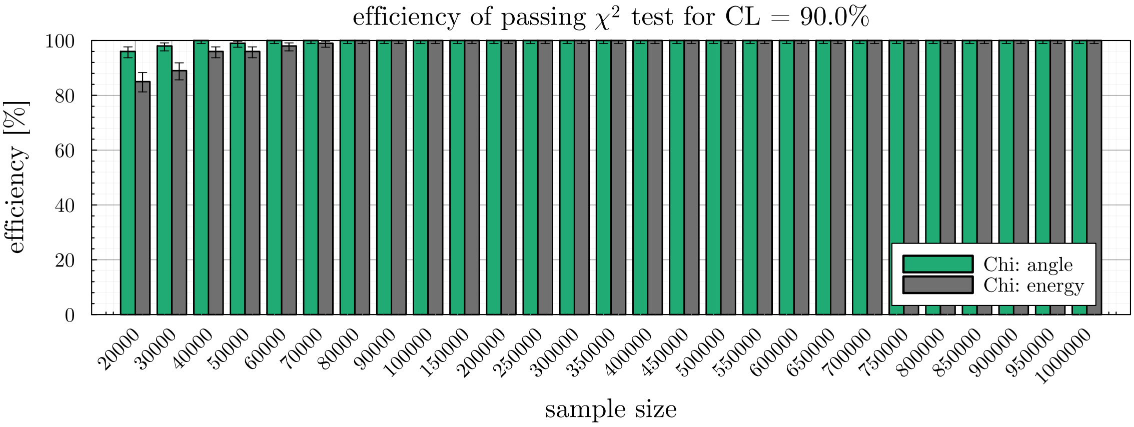

(b) ε_{reject,H_0} for χ^2 test at $CL = 90\%$.

Figure 6.9: Efficiencies for the KS and χ^2 tests at $CL = 90\%$. The best sample size is chosen such that the efficiency if 100% three times in a row.

CONCLUSION

The presented thesis explores the potential for investigating novel DBD physics within the SuperNEMO Experiment. **Chapter 1** provides a brief historical account of the neutrino postulate and subsequent discovery. It details the known neutrino properties and highlights some of the lingering questions. Some of these could be answered by thorough study of the mechanisms of DBD, as outlined in **chapter 2**. Here, the conventional approach to calculating $2\nu\beta\beta$ decay rates is presented. Furthermore, based on the works of [4, 5], an improved calculation is described. The introduction to new physics is presented through the proposed exotic DBD modes, which stem from BSM physics, outlined in **section 2.6**. Notably, the various processes share a common trait: a predicted changes in the shapes of angular and energy distributions, governed by either a single parameter or a collection of parameters encapsulating the novel physics.

The SuperNEMO detector, its design, and simulation software are detailed in **chapter 3**. The detector is currently in its final commissioning stages. Initial data collection runs have commenced, although the passive shielding is not yet fully installed. While, the option to turn on the magnetic field is available via the installed field-generating coil, the decision to turn it on has not yet been taken. It is anticipated that even after complete shielding installation, initial physics data collection runs will occur without activating the magnetic field.

Moreover, efforts are underway to develop an advanced track reconstruction algorithm. This algorithm, based on the Legendre transform, has the potential to considerably enhance the quality of reconstructed tracks.

The primary objectives of this thesis include investigating the detector's response to measurements of the opening angle between electrons and exploring new physics in the context of DBD. In **chapter 5**, the importance of understanding how the detector translates the unobservable decay angle into the measured escape angle, is outlined. The effects of the detector geometry are qualitatively summarized by reproducing the findings of [30] in a more generalized case of uniform spectra. It is found that the reconstruction is most successful for events of moderately open/closed angles, with tracks travelling approximately perpendicular to the source foil. Furthermore, the effects of the detector geometry far outweigh the underlying DBD physics in terms of the angular correlation. The chapter outlines the methodology for quantifying the detector response function using Monte Carlo simulated data. The potential improvements to the response function uncertainties through energy data-cuts or simplified unfolding methods are illustrated. Future prospects, such as analyzing scenarios with the magnetic field off or incorporating the new track reconstruction algorithm, are discussed. Although some benefits and some drawbacks are anticipated from turning off the magnetic field, the actual consequences remain uncertain. Notably, the primary outcome of **chapter 5** is the developed software, capable of computing the response function with its uncertainty, and performing basic unfolding. This software can be reapplied on arbitrary combination of input data and simulation settings.

Finally, **chapter 6** conducts a feasibility assessment of SuperNEMO. Here, the necessity for a framework that calculates the minimum number of events required for SuperNEMO to detect subtle predicted distinctions among various DBD modes is emphasized. This initial step is crucial to determine the feasibility of subsequent data fitting. By means of a simple toy model comparing an example set of standard and refined spectra, the methodology of statistical analysis is presented. The chapter's findings are promising, suggesting a minimum event count of approximately $10^4 - 10^5$ events, dependent on the chosen confidence level. This event count aligns well with SuperNEMO's data collection expectations. Additionally, the results suggest that the angular distribution serves as a more sensitive observable for study, surpassing the energy distribution. This emphasizes the advantage of SuperNEMO's unique tracker-calorimeter approach and underscores the importance of precise particle tracking systems. Concluding the chapter, plans for future expansion of the presented framework are discussed. This involves the incorporation of algorithms rooted in MLE approach for spectrum fitting. The decision whether to implement the approach of folding or unfolding will be investigated.

BIBLIOGRAPHY

1. Goeppert-Mayer, M. Double Beta-Disintegration. *Phys. Rev.* **48,** 512–516. `https://link.aps.org/doi/10.1103/PhysRev.48.512` (6 1935).
2. Abgrall, N. *et al. LEGEND-1000 Preconceptual Design Report* 2021. arXiv: `2107.11462 [physics.ins-det]`.
3. Nakamura, R. *et al.* Research and development toward KamLAND2-Zen. *Journal of Physics: Conf. Series* **1468,** 012256. `https://dx.doi.org/10.1088/1742-6596/1468/1/012256` (2020).
4. Simkovic, F. *et al.* Improved description of the $2\nu\beta\beta$-decay and a possibility to determine the effective axial-vector coupling constant. *Phys. Rev. C* **97,** 034315. `https://link.aps.org/doi/10.1103/PhysRevC.97.034315` (3 2018).
5. Nitescu, O. *et al.* Angular Distributions of Emitted Electrons in the Two-Neutrino $\beta\beta$ Decay. *Universe* **7.** ISSN: 2218-1997. `https://www.mdpi.com/2218-1997/7/5/147` (2021).
6. Deppisch, F. F. *et al.* Searching for New Physics in Two-Neutrino Double Beta Decay. *Phys. Rev. Lett.* **125,** 171801. `https://link.aps.org/doi/10.1103/PhysRevLett.125.171801` (17 2020).
7. Bolton, P. D. *et al.* Two-neutrino double beta decay with sterile neutrinos. *Phys. Rev. D* **103,** 055019. `https://link.aps.org/doi/10.1103/PhysRevD.103.055019` (5 2021).
8. Brown, L. M. The idea of the neutrino; Translation of W. Pauli's letter to Tübingen Conference, December 4, 1930. *Phys. Today* **31N9,** 23–28 (1978).
9. Das, A. & Ferbel, T. *Introduction to nuclear and particle physics* 2nd ed. ISBN: 9789812387448 (World Scientific, New Jersey, 2009).

10. Palusova, V. *Monte Carlo simulations of detectors background and analysis of background characteristics of the SuperNEMO experiment in the Modane underground laboratory* Theses (Universite de Bordeaux ; Comenius University in Bratislava, 2021). `https://theses.hal.science/tel-03521198`.
11. Cowan, C. L., Reines, F., *et al.* Detection of the Free Neutrino: a Confirmation. *Science* **124,** 103–104. eprint: `https://www.science.org/doi/pdf/10.1126/science.124.3212.103`. `https://www.science.org/doi/abs/10.1126/science.124.3212.103` (1956).
12. Xing, Z.-Z. & Zhou, S. *Neutrinos in Particle Physics, Astronomy and Cosmology* en. ISBN: 9783642175596 9783642175602. `https://link.springer.com/10.1007/978-3-642-17560-2` (2023) (Springer Berlin Heidelberg, Berlin, Heidelberg, 2011).
13. Gribov, V. & Pontecorvo, B. Neutrino astronomy and lepton charge. *Physics Letters B* **28,** 493–496. ISSN: 0370-2693. `https://www.sciencedirect.com/science/article/pii/0370269369905255` (1969).
14. Gribov, V. & Pontecorvo, B. Neutrino astronomy and lepton charge. en. *Physics Letters B* **28,** 493–496. ISSN: 03702693. `https://linkinghub.elsevier.com/retrieve/pii/0370269369905255` (2023) (Jan. 1969).
15. Lipari, P. *Introduction to neutrino physics* in *1st CERN-CLAF School of High-Energy Physics* (May 2001), 115–199.
16. Fukuda, Y. *et al.* Measurement of the Flux and Zenith-Angle Distribution of Upward Throughgoing Muons by Super-Kamiokande. *Phys. Rev. Lett.* **82,** 2644–2648. `https://link.aps.org/doi/10.1103/PhysRevLett.82.2644` (13 1999).
17. Ahmad, Q. R. *et al.* Direct Evidence for Neutrino Flavor Transformation from Neutral-Current Interactions in the Sudbury Neutrino Observatory. *Phys. Rev. Lett.* **89,** 011301. `https://link.aps.org/doi/10.1103/PhysRevLett.89.011301` (1 2002).
18. Gariazzo, S. *et al.* Neutrino masses and their ordering: Global Data, Priors and Models. *JCAP* **03,** 011. arXiv: `1801.04946 [hep-ph]` (2018).
19. Adrián-Martínez, S. *et al.* Letter of intent for KM3NeT 2.0. *Journal of Physics G: Nuclear and Particle Physics* **43,** 084001. `https://dx.doi.org/10.1088/0954-3899/43/8/084001` (2016).
20. Esteban, I. *et al.* Global analysis of three-flavour neutrino oscillations: synergies and tensions in the determination of θ23, δCP, and the mass ordering. en. *Journal of High Energy Physics* **2019,** 106. ISSN: 1029-8479. `https://link.springer.com/10.1007/JHEP01(2019)106` (2023) (2019).

21. Bilenky, S. M. & Petcov, S. T. Massive Neutrinos and Neutrino Oscillations. *Rev. Mod. Phys.* **59.** [Erratum: Rev.Mod.Phys. 61, 169 (1989), Erratum: Rev.Mod.Phys. 60, 575–575 (1988)], 671 (1987).
22. Majorana, E. Teoria simmetrica dell'elettrone e del positrone. *Nuovo Cim.* **14,** 171–184 (1937).
23. Zuber, K. Neutrino Physics. *Physics Today* **58,** 64–64. ISSN: 0031-9228. eprint: `https://pubs.aip.org/physicstoday/article-pdf/58/4/64/11175488/64\_1\_online.pdf`. `https://doi.org/10.1063/1.1955485` (2005).
24. Barabash, A. Precise Half-Life Values for Two-Neutrino Double-β Decay: 2020 Review. en. *Universe* **6,** 159. ISSN: 2218-1997. `https://www.mdpi.com/2218-1997/6/10/159` (2023) (2020).
25. Caurier, E. *et al.* Shell Model Studies of the Double Beta Decays of 76 Ge, 82 Se, and 136 Xe. en. *Physical Review Letters* **77,** 1954–1957. ISSN: 0031-9007, 1079-7114. `https://link.aps.org/doi/10.1103/PhysRevLett.77.1954` (2023) (1996).
26. Muto, K. *et al.* A comparative study of double beta decay by shell model and quasiparticle RPA. en. *Zeitschrift fur Physik A: Hadrons and Nuclei* **339,** 435–444. ISSN: 0939-7922, 1434-601X. `http://link.springer.com/10.1007/BF01288427` (2023) (1991).
27. Furry, W. H. On Transition Probabilities in Double Beta-Disintegration. *Phys. Rev.* **56,** 1184–1193. `https://link.aps.org/doi/10.1103/PhysRev.56.1184` (12 Dec. 1939).
28. Vergados, J. D. *et al.* Theory of Neutrinoless Double Beta Decay. *Rept. Prog. Phys.* **75,** 106301. arXiv: `1205.0649 [hep-ph]` (2012).
29. Engel, J. & Menéndez, J. Status and future of nuclear matrix elements for neutrinoless double-beta decay: a review. *Reports on Progress in Physics* **80,** 046301. `https://dx.doi.org/10.1088/1361-6633/aa5bc5` (2017).
30. Macko, M. *SuperNEMO Experiment : Study of Systematic Uncertainties of Track Reconstruction and Energy Calibration. Evaluation of Sensitivity to 0nbb with Emission of Majoron for Se-82.* PhD thesis (2018). `http://www.theses.fr/2018BORD0368/document`.
31. Petro, M. *Calculation of Sensitivity to Neutrinoless Double Beta-Decay for COBRA Demonstrator* MA thesis (University of Hradec Kralove, 2021).
32. Adhikari, G. *et al.* nEXO: neutrinoless double beta decay search beyond 1028 year half-life sensitivity. *Journal of Physics G: Nuclear and Particle Physics* **49,** 015104. `https://dx.doi.org/10.1088/1361-6471/ac3631` (2021).

33. Adams, C. *et al.* Sensitivity of a tonne-scale NEXT detector for neutrinoless double-beta decay searches. *J. High Energ. Phys.* **164** (2021).

34. Albanese, V. *et al.* The SNO+ experiment. *Journal of Instrumentation* **16,** P08059. `https://dx.doi.org/10.1088/1748-0221/16/08/P08059` (2021).

35. The CUORE Collaboration, Adams, D. Q., *et al.* Search for Majorana neutrinos exploiting millikelvin cryogenics with CUORE. en. *Nature* **604,** 53–58. ISSN: 0028-0836, 1476-4687. `https://www.nature.com/articles/s41586-022-04497-4` (2023) (Apr. 2022).

36. Armengaud, E. *et al. The CUPID-Mo experiment for neutrinoless double-beta decay: performance and prospects* 2020.

37. Arnold, R. *et al.* Probing new physics models of neutrinoless double beta decay with SuperNEMO. en. *The European Physical Journal C* **70,** 927–943. ISSN: 1434-6044, 1434-6052. `http://link.springer.com/10.1140/epjc/s10052-010-1481-5` (2023) (2010).

38. Lalanne, D. *et al.* Double-beta decay prototype detector with multiwire drift tubes in the Geiger mode. *Nuclear Physics B - Proceedings Supplements* **28,** 223–225. ISSN: 0920-5632. `https://www.sciencedirect.com/science/article/pii/092056329290175R` (1992).

39. Arnold, R. *et al.* NEMO experiment on double beta decay of 100Mo. Present status and future. *Nuclear Physics B - Proceedings Supplements* **35,** 369–371. ISSN: 0920-5632. `https://www.sciencedirect.com/science/article/pii/0920563294902798` (1994).

40. Arnold, R., Augier, C., *et al.* Technical design and performance of the NEMO 3 detector. *Nuclear Instruments and Methods in Physics Research Section A: Accelerators, Spectrometers, Detectors and Associated Equipment* **536,** 79–122. ISSN: 0168-9002. `https://www.sciencedirect.com/science/article/pii/S0168900204016821` (2005).

41. Arnold, R. *et al.* Detailed studies of ^{100}Mo two-neutrino double beta decay in NEMO-3. en. *The European Physical Journal C* **79,** 440. ISSN: 1434-6044, 1434-6052. `http://link.springer.com/10.1140/epjc/s10052-019-6948-4` (2023) (2019).

42. Bolton, P. D. *et al.* Two-neutrino double beta decay with sterile neutrinos. *Phys. Rev. D* **103,** 055019. `https://link.aps.org/doi/10.1103/PhysRevD.103.055019` (5 2021).

43. Deppisch, F. F. *et al.* Searching for New Physics in Two-Neutrino Double Beta Decay. *Phys. Rev. Lett.* **125,** 171801. `https://link.aps.org/doi/10.1103/PhysRevLett.125.171801` (17 2020).

44. Simkovic, F. *et al.* The single state dominance hypothesis and the two-neutrino double beta decay of 100Mo. *Journal of Physics G: Nuclear and Particle Physics* **27,** 2233. `https://dx.doi.org/10.1088/0954-3899/27/11/304` (2001).

45. Domin, P. *et al.* Neutrino accompanied $\beta^{\pm}\beta^{\pm}$, $\beta^{\pm}$/EC and EC/EC processes within single state dominance hypothesis. *Nuclear Physics A* **753,** 337–363. ISSN: 0375-9474. `https://www.sciencedirect.com/science/article/pii/S0375947405003519` (2005).

46. Doi, M. *et al.* Double Beta Decay. *Progress of Theoretical Physics* **69,** 602–635. ISSN: 0033-068X. eprint: `https://academic.oup.com/ptp/article-pdf/69/2/602/5252546/69-2-602.pdf`. `https://doi.org/10.1143/PTP.69.602` (1983).

47. Pati, J. C. & Salam, A. Lepton number as the fourth "color". *Phys. Rev. D* **10,** 275–289. `https://link.aps.org/doi/10.1103/PhysRevD.10.275` (1 1974).

48. Deppisch, F. F. *et al.* Supplemental Material: Searching for New Physics in Two-Neutrino Double Beta Decay. *Phys. Rev. Lett.* **125,** 171801. `https://journals.aps.org/prl/abstract/10.1103/PhysRevLett.125.171801#supplemental` (17 2020).

49. Arnold, R. *et al.* Probing new physics models of neutrinoless double beta decay with SuperNEMO. *The European Physical Journal C* **70,** 927–943 (2010).

50. Rakhimov, A. V. *et al.* Development of methods for the preparation of radiopure 82Se sources for the SuperNEMO neutrinoless double-beta decay experiment. *Radiochimica Acta* **108,** 87–97. `https://doi.org/10.1515/ract-2019-3129` (2020).

51. Barabash, A. *et al.* Calorimeter development for the SuperNEMO double beta decay experiment. *Nuclear Instruments and Methods in Physics Research Section A: Accelerators, Spectrometers, Detectors and Associated Equipment* **868,** 98–108. ISSN: 0168-9002. `https://www.sciencedirect.com/science/article/pii/S0168900217306976` (2017).

52. Hodák, R. *et al.* Improvement of the energy resolution of the scintillating detectors for the low background measurement. *AIP Conference Proceedings* **1672,** 130003. ISSN: 0094-243X. eprint: `https://pubs.aip.org/aip/acp/article-pdf/doi/10.1063/1.4928013/13721149/130003\_1\_online.pdf`. `https://doi.org/10.1063/1.4928013` (Aug. 2015).

53. Agostinelli, S. *et al.* Geant4—a simulation toolkit. *Nuclear Instruments and Methods in Physics Research Section A: Accelerators, Spectrometers, Detectors and Associated Equipment* **506,** 250–303. ISSN: 0168-9002. `https://www.sciencedirect.com/science/article/pii/S0168900203013688` (2003).

54. Ponkratenko, O. *et al.* Event Generator DECAY4 for Simulating Double-Beta Processes and Decays of Radioactive Nuclei. *Physics of Atomic Nuclei* **63.** Cited by: 173; All Open Access, Green Open Access, 1282–1287. `https://www.scopus.com/inward/record.uri?eid=2-s2.0-0034371636&doi=10.1134%2f1.855784&partnerID=40&md5=1f72b2555768c16610584655c84907d5` (2000).

55. Brun, R. & Rademakers, F. ROOT — An object oriented data analysis framework. *Nuclear Instruments and Methods in Physics Research Section A: Accelerators, Spectrometers, Detectors and Associated Equipment* **389.** New Computing Techniques in Physics Research V, 81–86. ISSN: 0168-9002. `https://www.sciencedirect.com/science/article/pii/S016890029700048X` (1997).

56. Macko, M. *MiModule for Falaise analysis version 1.0.0* `https://github.com/miroslav-macko/MiModule`.

57. Krizak, T. *Development of an algorithm for linear particle track reconstruction in SuperNEMO detector* Theses (Czech Technical University in Prague Faculty of Nuclear Sciences and Physical Engineering, 2023).

58. Kim, J. E. Light Pseudoscalars, Particle Physics and Cosmology. *Phys. Rept.* **150,** 1–177 (1987).

59. Quinn, W. *The sensitivity of the NEMO technique to neutrinoless double beta decay and the commissioning of the SuperNEMO demonstrator module* PhD thesis (University Coll. London, 2023).

60. Cowan, G. *Statistical data analysis* ISBN: 9780198501565 9780198501558 (Clarendon Press ; Oxford University Press, Oxford : New York, 1998).

61. Petro, M. *MPGenbb sampling package for 2ubb spectra version 1.0.0* `https://github.com/Shoram444/MPgenbb.jl`.

62. Cochran, W. G. The χ^2 Test of Goodness of Fit. *The Annals of Mathematical Statistics* **23,** 315–345 (1952).

63. Pearson, K. X. On the criterion that a given system of deviations from the probable in the case of a correlated system of variables is such that it can be reasonably supposed to have arisen from random sampling. *The London, Edinburgh, and Dublin Philosophical Magazine and Journal of Science* **50,** 157–175 (1900).

64. Kolmogorov, A. L. Sulla determinazione empirica di una legge di distribuzione. *Giornale dell'Istituto Italiano Degli Attuari* **4,** 83–91 (1933).

65. Smirnov, N. V. On the Estimation of Discrepancy between Empirical Curves of Distribution for Two Independent Samples. *Moscow University Mathematics Bulletin* **2,** 3–14 (1939).

66. Kornblith, S. & other contributors. *JuliaStats/HypothesisTests.jl v0.11.1* `https://github.com/JuliaStats/HypothesisTests.jl`.

67. Bezanson, J. *et al.* Julia: A fresh approach to numerical computing. *SIAM Review* **59,** 65–98 (Sept. 2017).

68. Paterno, M. Calculating efficiencies and their uncertainties. FERMILAB-TM-2286-CD (2004).

69. Gómez, H. *et al.* Latest results of NEMO-3 experiment and present status of SuperNEMO. *Nuclear and Particle Physics Proceedings* **273-275.** 37th International Conference on High Energy Physics (ICHEP), 1765–1770. ISSN: 2405-6014. `https://www.sciencedirect.com/science/article/pii/S2405601415007737` (2016).

APPENDIX A

APPENDIX A

A.1 List of Publications

1. **Theses**:
    (a) **M. Petro**, *Calculation of Sensitivity to Neutrinoless Double Beta Decay for COBRA Demonstrator* , Master Thesis, University of Hradec Kralove, Czechia, Faculty of Natural Sciences, 2021
    (b) **M. Petro**, *Investigating the physical properties of the ionic liquids PyR14TFSI doped with lithium salt and PyR18TFSI*, Bachelor Thesis, Roskilde University, Denmark, Department of Natural Sciences, 2017
2. **Articles**
    (a) ***SUBMITTED:*** **Measurement of double beta decay of ^{150}Nd to the 0_1^+ excited state of ^{150}Sm in NEMO-3**, Arnold, R., ..., **M. Petro**, and others, *submitted to Eur. Phys. J. C, 2023*
    (b) **Commissioning of the COBRA extended demonstrator at the LNGS**, J. Arling, L. Bodenstein-Dresler, ..., M. Macko, **M. Petro**, ..., K. Zuber, *Nucl.Instrum.Meth.A 1010 (2021) 165524*
    (c) **MIRAM - Miniaturized Radiation Monitor for Space**, Malich, M.; **Petro, M.**; Janeček, J.; Smetana, A.; Holík, M.; Bergmann, B.; Gohl, S.; Granja, C. et al., *Prototype, Functional Sample*
    (d) **Signal imaging from S-3-80-channel detector of reactor antineutrinos**, M. Slavickova, V. Belov, ..., **M. Petro**, ..., I. Stekl and I. Zhitnikov, *Journal of Instrumentation. 2020, 15 1-8. ISSN 1748-0221.*
3. **Proceedings**

(a) ***SUBMITTED:*** **M. Petro**, M. Macko, F. Šimkovic, *Probing the Refined Spectrum of* $2\nu\beta\beta$ *within the SuperNEMO Experiment*, Faculty of Mathematics, Physics and Informatics of Comenius University in Bratislava, submitted in April 2023

(b) ***SUBMITTED:*** **M. Petro**, M. Macko, F. Šimkovic, *Search for Exotic Modes of Double Beta Decay within the SuperNEMO Experiment*, MEDEX'22 Conference, Prague, submitted in September 2022

(c) **M. Petro**, M.Macko, J. Lipovský, *Calculation of Sensitivity to Neutrinoless Double Beta-Decay for COBRA Demonstrator*, Faculty of Mathematics, Physics and Informatics of Comenius University in Bratislava, ISBN 978-80-8147-127-8, p. 358, 2022